Fracture Behavior of Laser Powder Bed Fusion Fabricated Ti41Nb via *In-situ* Alloying

Sheng Huang [ab#], Punit Kumar [ab], Wai Yee Yeong [ab], R. Lakshmi Narayan [c] and Upadrasta Ramamurty [ad]

[a]School of Mechanical and Aerospace Engineering, Nanyang Technological University, 50 Nanyang Avenue, Singapore 639798
[b]Singapore Centre for 3D Printing, School of Mechanical & Aerospace Engineering, Nanyang Technological University, 50 Nanyang Avenue, Singapore 639798
[c]Department of Materials Science and Engineering, Indian Institute of Technology, Delhi, Hauz Khas, New Delhi, India 110016
[d]Institute of Materials Research and Engineering, Agency for Science, Technology and Research (A∗STAR), Singapore 138634.

#corresponding author: sheng007@e.ntu.edu.sg +65 9806 7027

Abstract: The microstructures and the mechanical properties, including fatigue crack growth (FCG) and mode I fracture toughness (K_{IC}), of *in-situ* alloyed Ti41Nb (wt.%) fabricated using the laser powder bed fusion (LB-PBF) were investigated. A small hatch spacing - fast scanning strategy was utilized for obtaining parts with minimum porosity and unmelted Nb particle combination. The mesostructure of the fabricated blocks comprises columnar grains with alternating Nb-poor regions (NPRs), which occur due to the short residence time of materials in the melt that limits the melting and diffusion of Nb, and matrix layers. Extensive ω_{iso} precipitates were noted in the microstructure, which were attributed to the large-build related heat accumulation during the LB-PBF process that stems from the combination of large sample size and high energy density input. Consequently, ductility of the as-built parts was low. The FCG rate at high ΔK was strongly influenced by the layers of NPR and hence depend on the orientation whereas the near-threshold FCG rate was strongly influenced by the local slip systems ahead of the crack tip. Significant anisotropy in K_{IC}, a result of the crack deflection by the NPR/matrix interfaces, was observed. The mesostructure induced toughening mechanism improves the fracture toughness of the resultant alloy despite its brittle failure response. The potential of *in-situ* alloying to induce toughening through the mesostructure control was discussed.

Keywords: Mechanical properties; Fatigue behavior; Fracture; Ti–Nb; Powder bed fusion.

1. Introduction

For load bearing biomedical implants, the mitigation of "stress shielding" is an important criterion. For this purpose, several low Young's modulus (E) β-Ti alloys that contain non-toxic elements such as Ti, Nb, Ta were developed. The $Ti_{53.4}Nb_{29}Ta_{13}Zr_{4.6}$ (composition in wt.%) alloy, known as TNTZ, is a widely explored β-Ti alloy as it exhibits low E ~64 GPa (whereas E of commonly used implant materials such as CP Ti and Ti64 is ~110 GPa), good yield strength (YS > 500 MPa), and high strain to failure (ε_f > 20%) in the cold rolled and solutionized state [1]. However, its E is almost-twice that of the cortical bone (~30 GPa), which is the stiffest part of the bone. The recent advances in the additive manufacturing (AM) technologies such as the laser powder bed fusion (LB-PBF) provide an opportunity to incorporate cellular structures into the manufactured biomedical components such that their structural stiffness matches with that of the bone [2]. Newer generations of β-Ti alloys that are tailored for AM would allow for bespoke design and improved osseointegration characteristics of the biomedical implants.

While research on LB-PBF fabricated β-Ti alloys is actively pursued, the availability of pre-alloyed feedstock remains a major challenge for exploring different alloy compositions. As the small batch production for alloy powders is expensive, *in-situ* alloying via LB-PBF of blended powders could be advantageous due to the flexibility it offers for preliminary screening of different alloy compositions [3-7]. Towards this end, the effectiveness of *in-situ* alloying to produce Ti26Nb (at.%) with low porosity < 1% and sufficient homogeneity had been demonstrated [7]. A combination of E ~ 89 GPa and YS ~1029 MPa was obtained in *in-situ* alloyed Ti25Ta (wt.%) [8]. Its scaffolded implant exhibits superior biocompatibility to that of scaffolded CP Ti implant [9]. With *in-situ* alloying, components with compositional gradations can also be fabricated, which will expand the design space considerably [10]. Despite these advantages, *in-situ* alloying is not meant to replace LB-PBF using pre-alloyed powder. For instance, additional efforts are required to optimize the powder characteristics and blending techniques in order to improve the compositional homogeneity of *in-situ* alloyed product, albeit still inferior to those fabricated with pre-alloyed powder [11]. Moreover, the optimized energy density (E_d) for the production of Ti-Nb alloy (of similar composition) is far lesser with the usage of pre-alloyed feedstock, as opposed to those with *in-situ* alloying technique (40 J/mm^3 [12] vs. 214 J/mm^3 [7]). The additional energy input is required to improve the product's homogeneity, which could lead to melt overflow that compromises surface finish of the

resultant product. The need to simultaneously achieve homogenization, porosity minimization, and good surface finish can add significant complexity to the process of identifying the optimum process window, while it is relatively straight forward when pre-alloyed powders are utilized.

A common feature in *in-situ* alloyed β-Ti is the occurrence of compositional macro-segregation due to incomplete melting and diffusion of β-stabilizing particles [4, 13], caused by the short residence time of materials in the melt that stems from the high cooling rate intrinsic to the LB-PBF process (~10^6 K/s) [14]. Such features enhance the microstructural complexity of the printed parts, which also will have a mesostructure that manifests from the scan and hatch strategies adapted. All these could affect the mechanical behavior of the part, in particular the fracture and fatigue crack growth (FCG) characteristics [15], which are paramount in the context of reliability and service life of a biomedical implant. However, these aspects of *in-situ* alloyed β-Ti were not explored in detail hitherto. The only study, conducted by Brodie et al. [16] on the low cycle fatigue behavior of Ti25Ta (wt %), reports that unmelted Ta particles do not contribute to the fatigue crack initiation of the material. Prior studies on LB-PBF on other alloy systems have shown that the mesostructures are beneficial in improving their fracture and FCG responses [17-19]. For instance, the wavy melt pool boundaries in Al12Si and AlSi10Mg imparts high crack tortuosity and toughens the resultant material [17, 18]. Likewise, the prior β columnar grains in Ti6Al4V alloy enhances its toughness by deflecting the cracks when they are propagating perpendicular to the build direction (BD) [19]. Keeping these in view, the fracture and FCG behavior of the *in-situ* alloyed LB-PBF Ti41Nb were examined in detail in this study.

2. Materials and experiments

2.1. Materials

The Ti41Nb specimens examined in this study were fabricated using the gas atomized commercially pure (CP) Ti and 41 wt.% Nb (> 99.8% purity) elemental powder blends. The CP Ti powder (Grade 2 ASTM B348 [20], LPW Technology Ltd, United Kingdom) particles have a median diameter of 43.5 μm while the Nb powder (Tecnisco Advance Material Pte Ltd, Singapore) has a particle size distribution that ranges between 20 and 63 μm. The powders were mixed and blended for 12 hours under an argon atmosphere in a tumbler mixer rotating at a rate of 30 rpm. LB-PBF was carried out on Ti base plates and in an argon environment

(oxygen < 1000 ppm) with a SLM 280 HL system (SLM Solutions Group AG) equipped with a dual fibre laser system, with each laser having Gaussian beam profile (1064 nm) of a focus diameter of 80 µm and a maximum laser power of 400 W. The rotated stripe scanning strategy, schematically illustrated in Figure 1, is used. The stripes are rotated clockwise by ~79^{o} with respect to the previous layer in every subsequent new layer. The "Skywriting" strategy was enabled during the fabrication process, which allows constant laser scanning speed to be achieved throughout the intended scan region [21]. This can be achieved by isolating the acceleration and deceleration phase of the deflection mirrors from the intended scan path. This enables the turning on of the laser beam only during the constant laser scan speed phase.

Four different parameter sets (Table 1) were explored for process optimization that would lead to specimens with low porosity as well as minimum unmelted Nb powder particles. In all the four cases, the same laser power (P) of 390 W, stripe width of ~1 mm, layer thickness (t) of ~50 µm and scan rotation of ~79^{o}. were used. For each parameter set, the nomenclature is based on the associated E_d and the hatch spacing (h). The lables "L" and "H" stands for low and high E_d respectively, while the "20" and "40" are the values of h in µm.

During the *in-situ* alloying of Ti-Nb, a high energy input reduces the unmelted Nb but enhances keyhole porosity, leading to the inclusion-porosity dilemma [22]. The usage of top-hat profiled laser to manipulate the melt pool behavior can circumvent this. Instead of the typical scanning strategy that employs h close to the laser focus diameter (see Figure 1b), an alternative strategy that uses a small h -fast scan velocity (V_L) combination (see Figure 1a) with the commonly available 400 W Gaussian profiled laser is used in the present work. Among the four parameter combinations explored, the optimum combination of density and homogeneity was obtained in the case of H20, which was used to print blocks of 40 mm length, 35 mm width and 35 mm height.

The printed blocks were cut into multiple tensile and Chevron notched compact tension C(T) (thickness (b) 12 mm and width (W) 24 mm) test specimens using wire electric discharge machining (EDM). The orientations of the specimens in relation to those of the printing are schematically illustrated in Figure 2, where the building direction (BD) coincides with the z-axis. C(T) specimens with three different crack growth directions with respect to the BD were tested, so as to evaluate the anisotropy in K_{IC} and FCG characteristics. Two of them are referred to as ⊥, and ∥ for crack growth directions perpendicular, and parallel to BD, respectively. In the

third type, which lay in the XY plane with crack growing perpendicular to BD, is referred to as L.

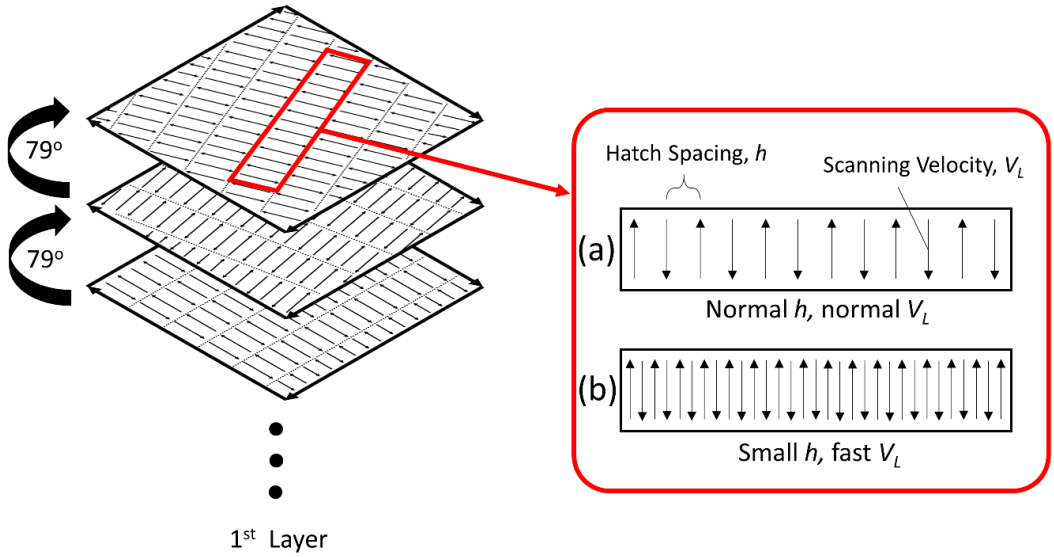

Figure 1. Schematic diagram of rotating stripe strategy used, with stripe scanning corresponding to (a) normal h - normal V_L and (b) fast h - fast V_L strategies.

Table 1 Different combinations of LB-PBF process parameters utilized for manufacturing the Ti41Nb alloy samples.

Designation	**Hatch spacing, *h* (µm)**	**Scan velocity, V_L (mm/s)**	**Energy density, E_d (J/mm^3)**	**Porosity vol. fraction, $V_{f,p}$ (%)**	**Unmelted Nb vol. fraction, $V_{f,Nb}$ (%)**
L20	20	1147	340	0.010 ± 0.003	0.440 ± 0.025
H20	20	951	410	0.045 ± 0.008	0.391 ± 0.043
L40	40	574	340	0.066 ± 0.003	0.594 ± 0.035
H40	40	476	410	0.172 ± 0.010	0.426 ± 0.033

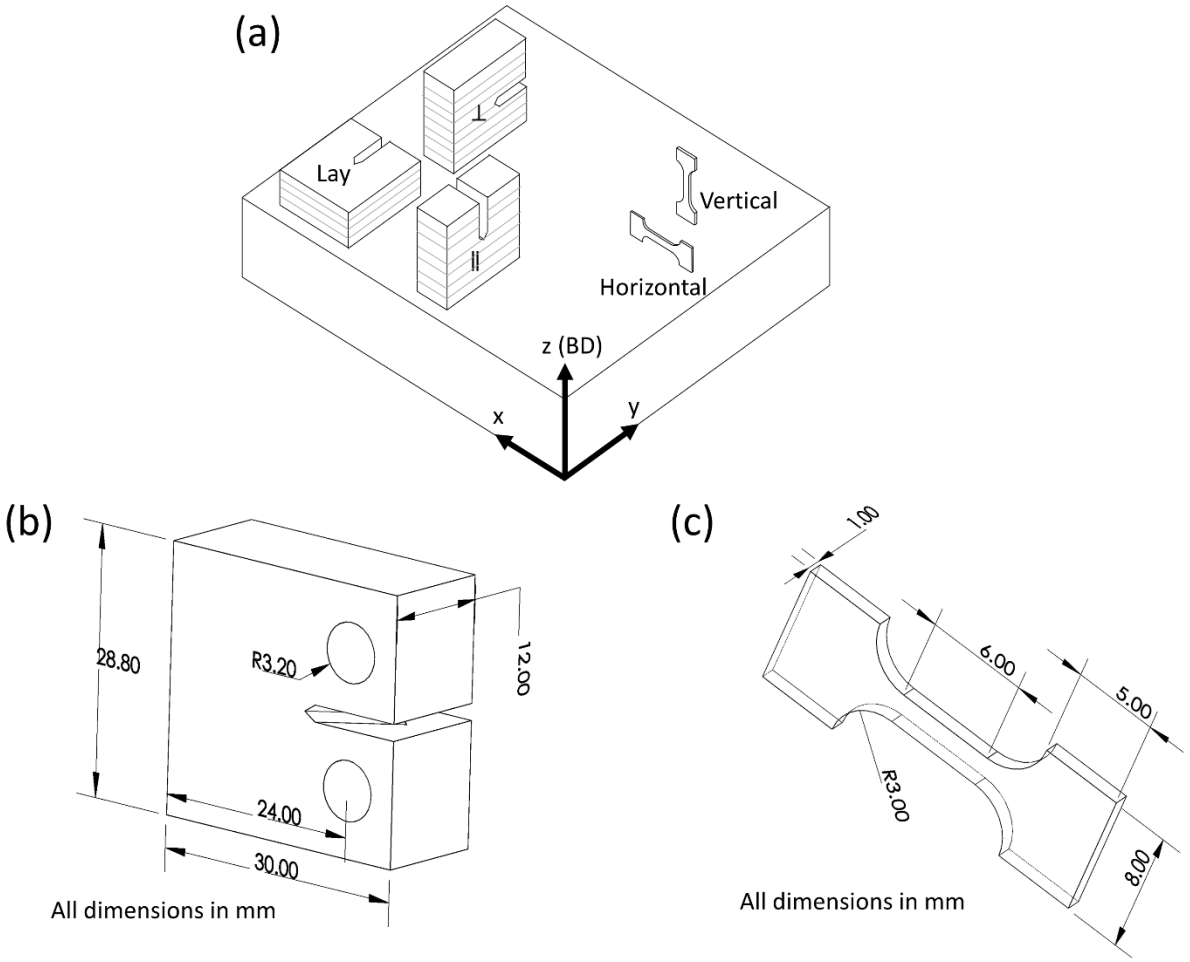

Figure 2. Schematic diagrams showing (a) the different orientations of test specimens with respect to the BD, and the dimensions of (b) C(T) and (c) tensile specimens.

2.2. Experiments

The microstructure of the specimens was examined in the cross-sections that are parallel and perpendicular to the BD. For the microstructural evaluations, the specimens were mirror polished using successively SiC-paper, suspensions of 9 μm diamond and 0.04 μm $SiO_2 + H_2O_2$. The micro- and meso-structures of the polished specimens were characterized using optical microscopy (OM) and scanning electron microscopy (SEM). Energy dispersive X-ray spectroscopy (EDS) was used to ascertain the compositions of various regions of the specimens. X-ray diffraction (XRD) with a Cu-source (step size of 0.05°) was used to identify the overall constituent phases in the specimens. To analyze the texture, electron backscatter diffraction (EBSD) mapping with a maximum step size of 1.5 μm was performed using AZtecHKL Oxford detector mounted on the scanning electron microscope. Transmission electron microscopy

(TEM) was performed on samples that were prepared using the focused ion beam (FIB) lift out technique.

The percentage volume fractions of the pores and the un-melted Nb particles in the as-built specimens were analyzed by recourse to X-ray computed tomography (XCT) (SKYSCAN 1173, Bruker, Germany) operating at a voltage of 130 kV, using a brass filter. The 3D reconstructed volumes are made up of isotropic cube voxels with a side length of 5.7 μm. To minimize the probability of false segmentation, only pores/inclusions with at least 9 voxels were considered. Three threshold values were taken during the analysis to account for the error [23], by which the standard errors were obtained.

Uniaxial tensile tests were performed as per the ASTM-E8 [24] standard on an universal testing machine (UTM) equipped with a laser extensometer and at a crosshead velocity of 0.006 mm/min. A minimum of three tests were conducted for each orientation. The K_{IC} and FCG tests were conducted on two specimens for each condition. Prior to the tests, both sides of the C(T) specimens were mirror polished to monitor the crack growth using a high-resolution camera attached on a long-distance optical microscope capable of 60X magnification. For evaluating K_{IC}, the specimens were fatigue pre-cracked using a servo hydraulic testing machine until the crack length (a) is such that a/W ~0.45-0.55. For pre-cracking, a sinusoidal wave form with a frequency of 10 Hz at a load ratio, R, of 0.1 was used, as prescribed in ASTM E399-12 [25] and ASTM 647-15 [26]. After the pre-cracking, the specimens were quasi-statically pulled until fracture at a crosshead displacement rate of 0.002 mm/s.

The threshold stress intensity factor range (ΔK_o) for FCG was determined using the load shedding method recommended in ASTM 647-15. For measuring ΔK_o, the stress intensity factor range (ΔK) was reduced by ~10% after each crack length increment of 0.2 mm, until the crack growth rate per cycle, da/dN, is below ~4 x10^{-9} m/cycle. The da/dN vs. ΔK data generated during the steady-state crack growth regime was analyzed using the Paris equation: $da/dN = C(\Delta K)^m$ (after discounting for the initial a of ~6 mm to nullify the notch effect), where C and m are material properties and are referred to as Paris constant and Paris exponent, respectively. Postmortem fractography were performed on the tensile fractured coupons, fatigue pre-cracked C(T) specimens, and mode-I fractured C(T) specimens using SEM. EDS was also performed on the fracture surfaces of the tensile specimens to ascertain the effect of compositional segregation on fracture behavior. Postmortem EBSD (maximum step size ~1.5 μm) and BSE

analyses were performed on the side surfaces of the tensile coupons and pre-cracked C(T) specimens.

3. Results

3.1. Parameter optimization

The combination of P, h, t and V_L, i.e., $E_d \sim (P/h.t.V_L)$ is the most commonly used parameter for LB-PBF process parameter optimization [27]. However, the porosity-inclusion dilemma for *in-situ* alloying of elements with significant melting point differences, e.g., Ti (1668 ^oC) and Nb (2477 ^oC), introduces an additional complexity. An increase in E_d does reduce the amount of unmelted Nb particles to some extent. However, it also leads to formation of keyhole porosity. Such a phenomenon have been also observed during LB-PBF *in-situ* alloying of other Ti-alloys such as Ti-Ta [4]. Therefore, innovative melt-pool strategies are required [22]. The melt pool manipulation approach used in this study was guided by the normalized enthalpy [28], which is proportional to $P/\sqrt{V_L}$, consideration with the assumption of constant material properties and laser specifications. By reducing $P/\sqrt{V_L}$ through a faster V_L, the tendency of keyhole melting can be suppressed. To compensate for the consequent lower energy input, h is reduced as to maintain E_d at the essential level for homogenization of the alloy. This attempt to reduce $P/\sqrt{V_L}$ ratio while maintaining E_d led to a 6.6-fold porosity reduction from H40 to H20, and a 3.8-fold porosity reduction from L40 to L20 (see Table 1). At the same time, minor reduction in the volume fraction (V_f) of the unmelted Nb can be also observed, indicating the effectiveness of this modified strategy. This improvement could be due to the thorough re-melting of the material, which enhanced the residence time of Nb particles in the melt and facilitates their effective melting and diffusion. Since this method utilizes a commonly available laser system with Gaussian profile, it is applicable to other LB-PBF systems in general.

Figure 3 shows the reconstructed XCT images of all the four sets of specimens printed for the parameter optimization; estimated values of respective V_f are also displayed. Due to the relatively large E_d used (~360 and 410 J/mm^3), pores are mostly of keyhole type. Furthermore, the XRT analyses shows that the specimens printed using H20 parameter have the least unmelted Nb (V_f of ~0.391%) while having >99.95% density. In the case of H20, where E_d was held constant, V_L is twice that of H40, demonstrating that the small h - fast V_L strategy in

effective in addressing the porosity-unmelted inclusion dilemma, without varying E_d. Thus, H20 was selected to print bigger blocks for the mechanical property evaluation.

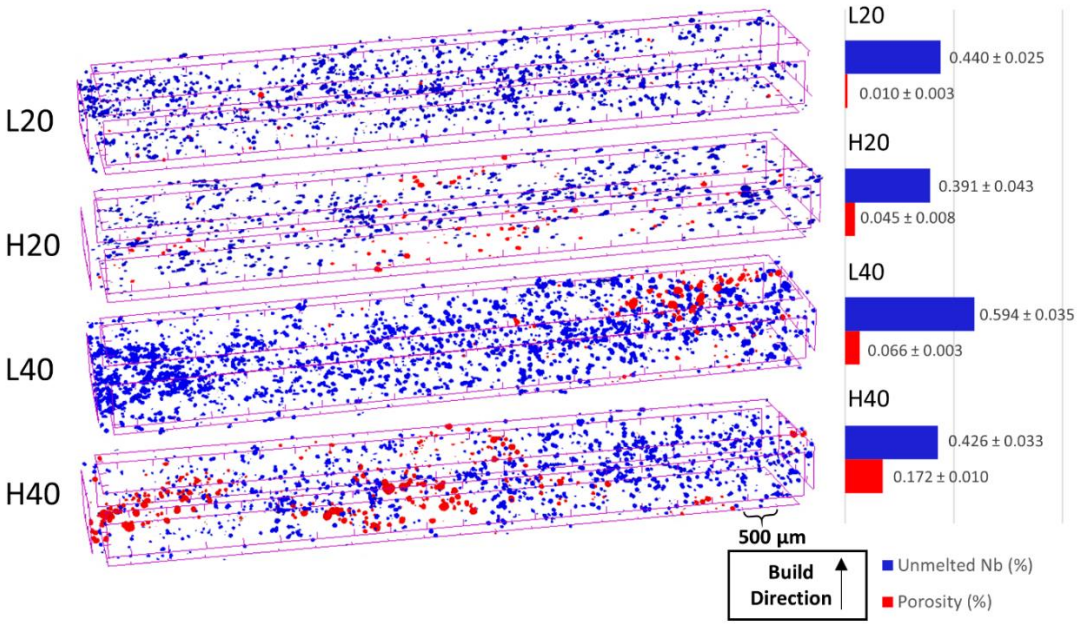

Figure 3. Three dimensional XCT images showing the distribution of unmelted Nb particles (blue) and porosity (red) in the L20, H20, L40 and H40 samples. Quantitative estimates (confidence interval of 99.7%) of them in each sample are summarized in the bar charts.

3.2. Micro- and meso-structures

EDS maps (not shown) that encompass the matrix as well as the unmelted Nb inclusions show the Nb content in the printed alloy was ~41.2%, which is within ± 0.5% of the targeted composition. The XRD scan obtained on the as-printed H20 block is displayed in Figure 4. All the diffraction peaks in it correspond solely to the body centered cubic (BCC) phase, indicating the stabilization of β-Ti. The thermodynamically stable phases for Ti41Nb at room temperature according to the Ti-Nb phase diagram [29] are hexagonal close packed (HCP) α and β (BCC). Usually, stabilized β-Ti is obtained only when the temperature is above the β transus (~620 ^{o}C). However, if the cooling rate is suitably adjusted, metastable β phase can be fully retained at lower temperatures, which might be accompanied with minute amount of other metastable phase such as the ω phase. In the present case, β phase was fully retained at room temperature because of fast cooling rates associated with the LB-PBF process.

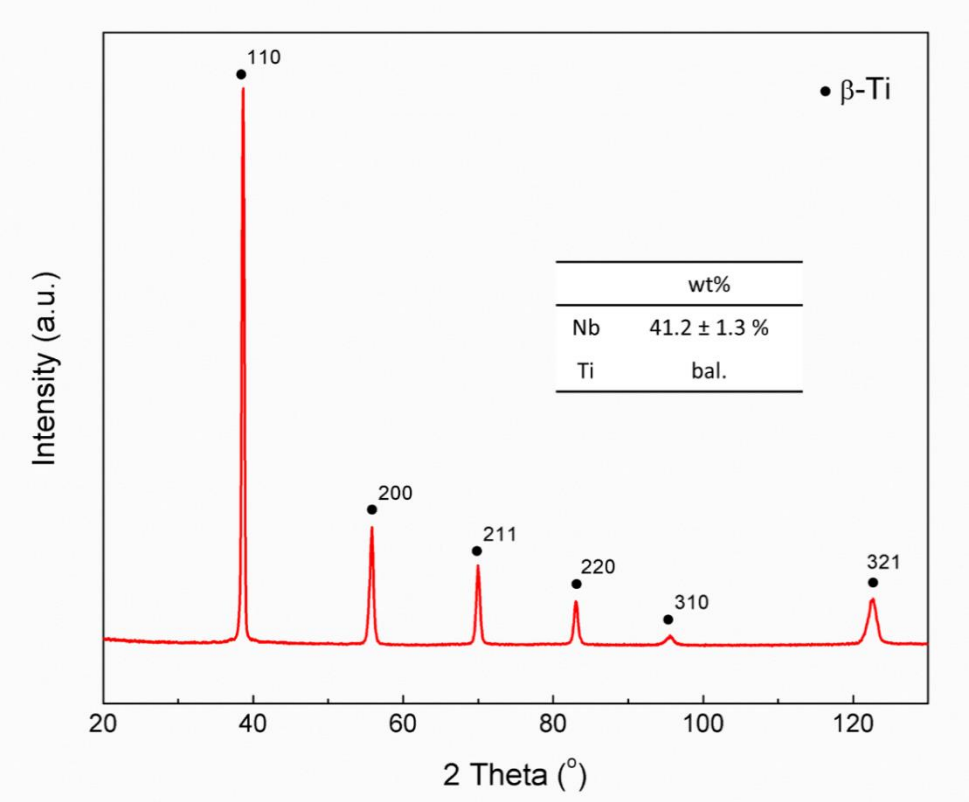

Figure 4. Phase and elemental constituents of the in-situ alloyed Ti41Nb alloy via LB-PBF.

Figure 5 shows a representative banded mesostructure of H20 specimens, while Figure 6 shows the representative micro- and meso-structures in it at different length scales. Under the BSE imaging mode, the mesostructure of *in-situ* alloyed Ti41Nb can be visualized due to the compositional contrast, as seen in Figure 5 and Figure 6a. Being a binary alloy, the brighter pixel in a BSE image represents higher Nb concentration. Usually, the unmelted Nb particles are distributed randomly in the printed specimens. However, the compounding effect of the process parameter utilized for H20 (high E_d, small h and high v) and the relatively high melting point and density of Nb, led to settling and (subsequent) freezing of its particles near the melt pool boundary, prematurely halting the homogenization process via Marangoni convection and diffusion at the bottom of the melt pool of each layer. Apart from that, complete chemical homogeneity was observed in other parts of the melt pool due to high E_d. This resulted in the formation of banded mesostructure with alternating Nb poor and homogenized layers, in which the latter (or matrix) layers have close-to-nominal composition. The Nb poor layer is often accompanied by an incompletely diffused Nb particle. Columnar grain structure was also observed (Figure 6b); such columnar structure is typically associated with the usage of a high

E_d during the manufacturing of metastable β-Ti via LB-PBF or any alloy with cubic crystal structure [7, 30].

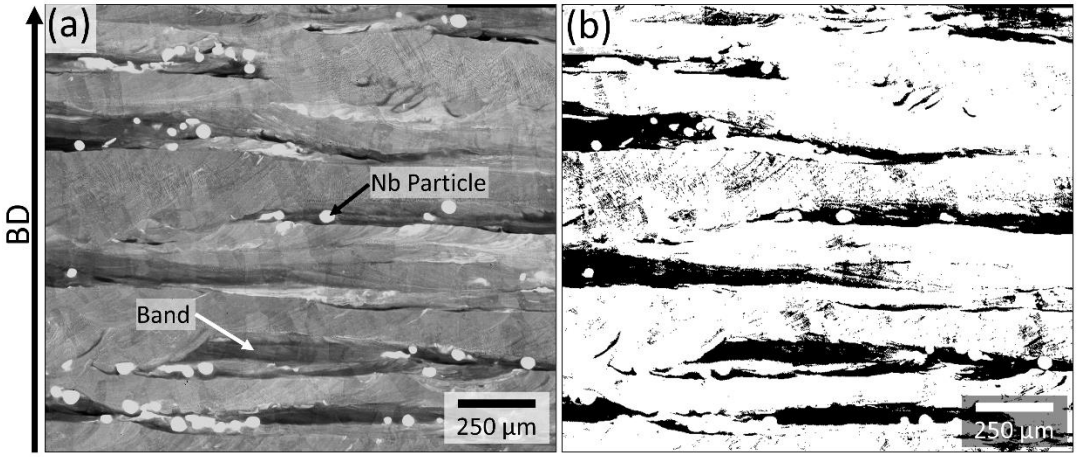

Figure 5. (a) Representative BSE image depicting banded mesostructure of H20 specimens. (b) Thresholded image of (a) to highlight the banded mesostructure.

A closer examination of the matrix regions reveals cellular microstructure induced by constitutional supercooling (Figure 6c) — a feature commonly seen in the LB-PBF manufactured parts [31]. The orthorhombic α'' phase was occasionally found in the Nb-poor regions (NPR) as seen in Figure 6d, which is a metastable phase typically observed in TiNb alloys with approximately 20 to 35 wt.% Nb [32, 33]. However, XRD analysis did not reveal any α'' peaks, possibly due to its low volume fraction.

TEM was carried out on the matrix region to investigate the nanostructure of the as-built sample. The selected area diffraction (SAED) pattern displayed in Figure 6e reveals the presence of isothermal ω phase (ω_{iso} phase) in the microstructure. It was identified on the basis of sharp ω spots in the SAED pattern, which form due to the complete collapse of {111} β planes, which occurs upon isothermal annealing of the metastable β-Ti alloy [34]. This can be differentiated from the athermal ω_{ath} phase that exhibits displacive partial collapse of {111} β planes, which would result in fuzzy streaks in the SAED image, as observed in the metastable β-Ti that was quenched from the high-temperature β phase field [34-36]. The conventional XRD technique used in this study does not have the necessary sensitivity to detect the ω_{iso} phase and requires the usage of synchrotron XRD to detect them [37]. The dark field image of the ω_{iso} phase is displayed in Figure 6f. It shows homogeneously distributed nanoscale precipitates with a mean size of < 4 nm.

The width of the grains and the {100} pole figure obtained using EBSD performed on the H20 specimens are plotted in Figure 7a and b, respectively. The mean grain width (~148.9 μm) in the present case is bigger compared to those reported (<100 μm) in the past for *in-situ* alloyed TiNb [7, 30]. This is due to relatively higher E_d ~410 J/mm^3 utilized in comparison to the past studies where the maximum E_d used is 291.67 J/mm^3. A high E_d can lead to larger extent of remelting, facilitating coarsening of the grains. The observation of a strong {100} fiber texture implies that the grains have preferential {100} orientation along the BD. The fiber texture could be beneficial for implant applications requiring low *E*, as β-Ti possesses minimum *E* along the <100> loading direction [38]. The multiples of uniform density (MUD) value describes the relative strength of a specific orientation with respect that of the randomized grain orientation, which is also referred to as the 'texture strength'. In present case, a MUD value of 7.42 was obtained for the {100} texture.

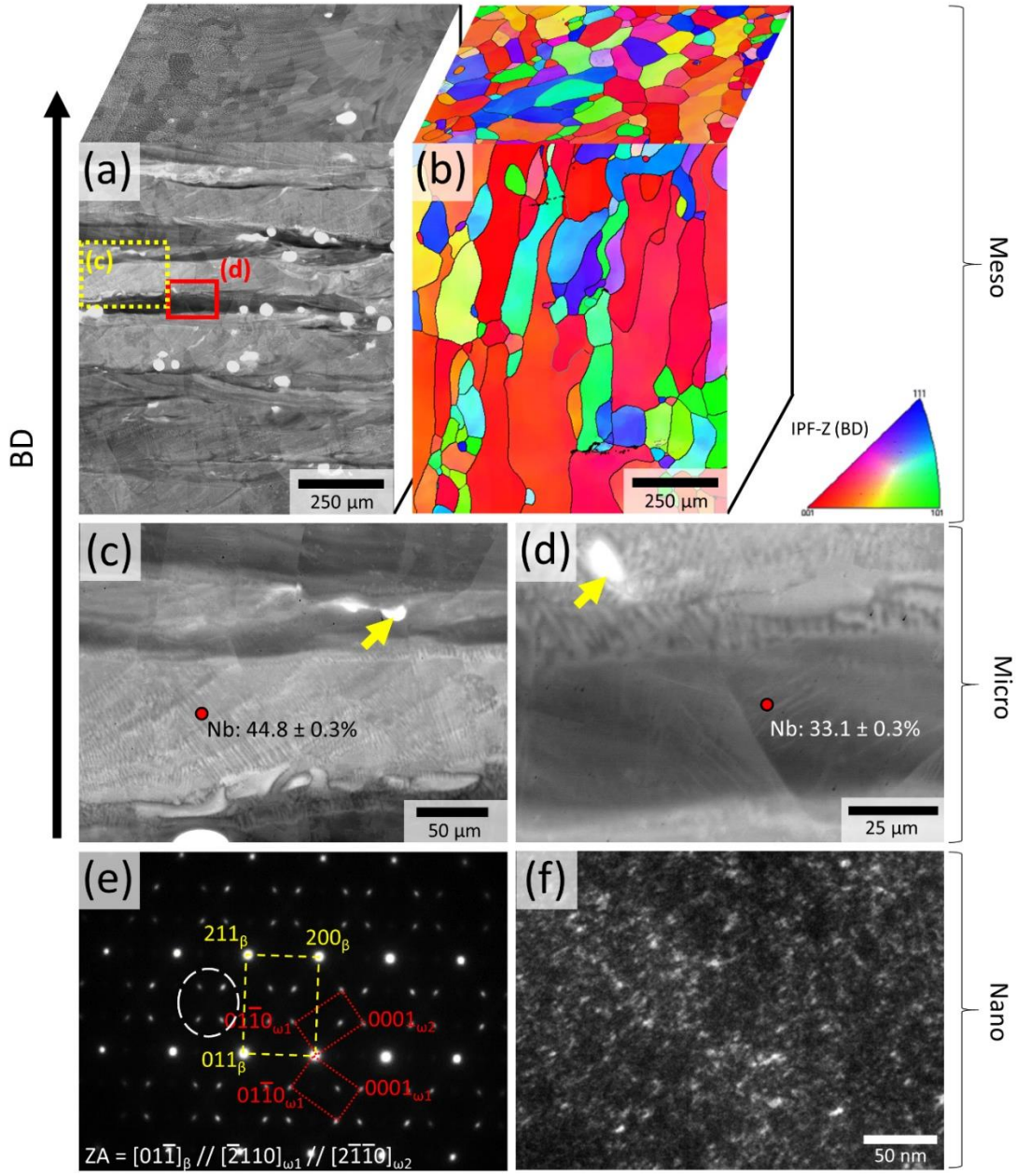

Figure 6. (a) BS image and (b) grain orientation map (with IPF-Z coloring) illustrating the mesostructure of the in-situ alloyed Ti41Nb part. (c) and (d) Magnified images of the matrix and the Nb depleted regions, respectively. (e) SAED and (f) bright field TEM images of the ω1 and ω2 variants. Arrows in (c) and (d) point towards unmelted Nb particles. The white discontinuous circle in (e) is the SAED pattern used for the dark field TEM image. The zone axis (ZA) of TEM image is given at the bottom of image (e).

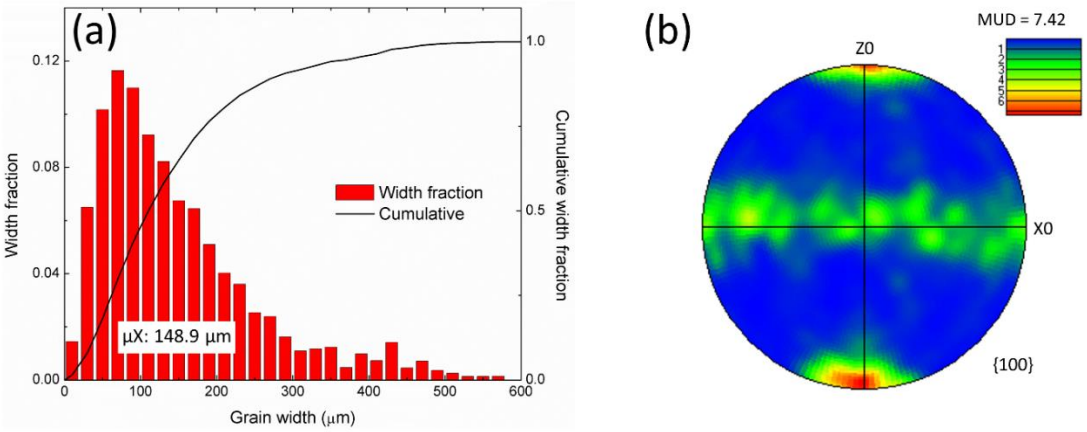

Figure 7. (a) Grain width distribution and (b) the {100} pole figure of the in-situ alloyed Ti41Nb via LB-PBF.

3.3. Tensile properties

Tensile tests were performed on specimens with the loading direction either perpendicular or parallel to BD; these are referred to as the horizontal and vertical tensile coupons, respectively. Their representative engineering stress, σ, and engineering strain, *e*, responses are displayed in Figure 8. The values of YS, UTS, *E* and elongation to failure, e_f obtained are listed in Table 2. Both the tensile responses show negligible plasticity with $e_f < 2\%$, which is significantly lower than those reported ($e_f > 8\%$) for conventionally and LB-PBF manufactured TiNb alloys [30, 39, 40]. This brittle response is accompanied by relatively large specimen-to-specimen variation in the UTS for the same tensile orientation. In between the two orientations, marginally higher e_f and lower *E* and YS was noted in the vertical orientation. The marginal difference in *E* was surprising, given the fiber texture in the coupons, which was expected to impart strong anisotropy to *E* [38]. The measured values of *E* (76.3 and 74.1 GPa) and YS (~814 and 785 MPa) are significantly higher than that (~60 GPa and ~675 MPa) of LB-PBF Ti42Nb (wt.%) manufactured using pre-alloyed feed stock [12].

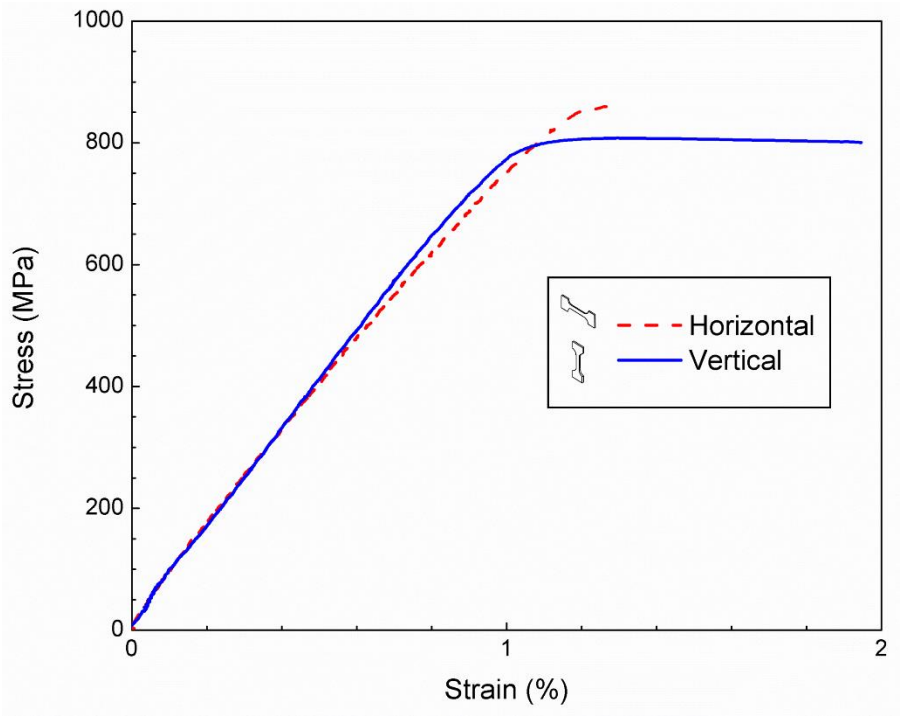

Figure 8. Representative tensile stress-strain response of horizontal and vertical tensile coupon.

Table 2 Tensile properties of horizontal and vertical tensile coupon. All values are quoted with confidence interval of 99.7%.

Orientation	**YS (MPa)**	**UTS (MPa)**	***E* (GPa)**	**e_f (%)**
Horizontal	814 ± 69.3	830 ± 117.2	76.3 ± 7.1	1.43 ± 0.9
Vertical	785 ± 31.6	787 ± 32.0	74.1 ± 8.5	1.65 ± 0.5

Figure 9 shows the representative fractographs obtained from the tensile tested specimens. Cleavage dominates the fracture morphology in both the orientations, consistent with the brittle stress-strain responses measured. Cleavage of the columnar grains can be seen on the fracture surface of the horizontal specimen, suggestive of the effect of grain morphology on the tensile properties. Stress localization in the layers rich with unmelted Nb particles could be one possibility behind the early failure of the tensile coupons [13]. EDS maps obtained on the fracture surfaces are displayed in Figure 9c and d. In both the cases, the fracture surface cleaved across only a few Nb particles, implying that unmelted Nb particles are not the cause for the poor ductility observed.

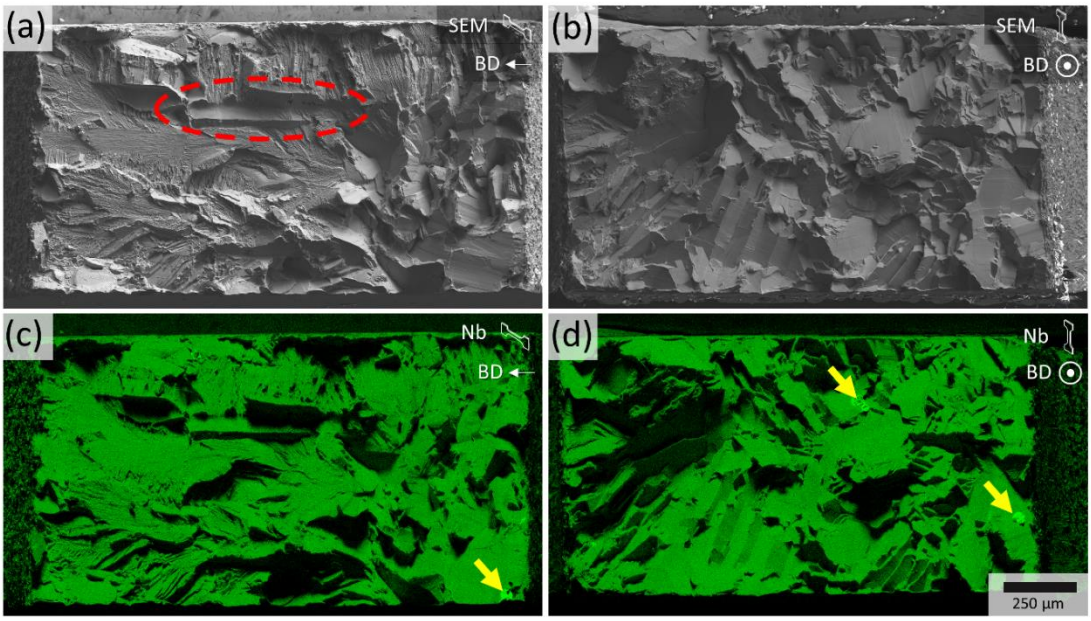

Figure 9. Representative fracture morphologies of (a) horizonal and (b) vertical tensile tested specimens, and (c) and (d) their respective Nb EDS maps. Red dotted circle in (a) highlights the cleavage of an elongated grain. Yellow arrows point incompletely melted Nb particles.

Postmortem analyses of the side surfaces of the fractured tensile specimens shows the absence of secondary cracks on the horizontal specimen (Figure 10a) whereas multiple secondary cracks growing below the fracture surface were seen on the vertical specimen (Figure 10b). EBSD maps of these regions are displayed in Figure 10c and d, respectively. The formation of stress induced martensite (SIM) and twins, which were identified as the {332}<113> variants on the basis of the rotation angle (~50.5^{o}) between the twin and matrix lattices [41], were noted on the horizontal coupon while the vertical specimens did not show any such features. Overall, the formation of α'' SIM / twining / dislocation slip was insignificant in both directions due the presence of ω_{iso} phase [41, 42]. The suppression of all the mechanisms responsible for plastic deformation resulted in the brittle failure of the tensile coupons by cleavage.

While a mixture of transgranular and intergranular facture was observed for the horizontal coupon, transgranular fracture dominates in the vertical coupons. The ω_{iso} precipitates only allow dislocation slip along isolated {112} slip planes, which possibly contribute to the localized planar deformation bands in β-Ti alloy [42]. Stress concentration caused by the pile ups at the grain boundaries can lead to cleavage initiation. In the horizontal samples, the grain boundaries are perpendicular to the tensile loading direction which facilitates early

intergranular fracture. It is difficult, however, when the direction of tensile stress is parallel to the long columnar grains, which is why the vertical coupon can sustain a marginally higher plastic deformation prior to failure. It is also important to note that the sub-surface transgranular fracture in the vertical specimen occurs predominantly along the {112} slip planes (see Figure S1 in Supplementary Information). In conjunction with the poor ductility, the suppression of dislocation slip by the ω_{iso} phase enhanced the YS. At the same time, ω_{iso} is also responsible for the stiffening and the reduction of anisotropy of *E* in the H20 sample [43].

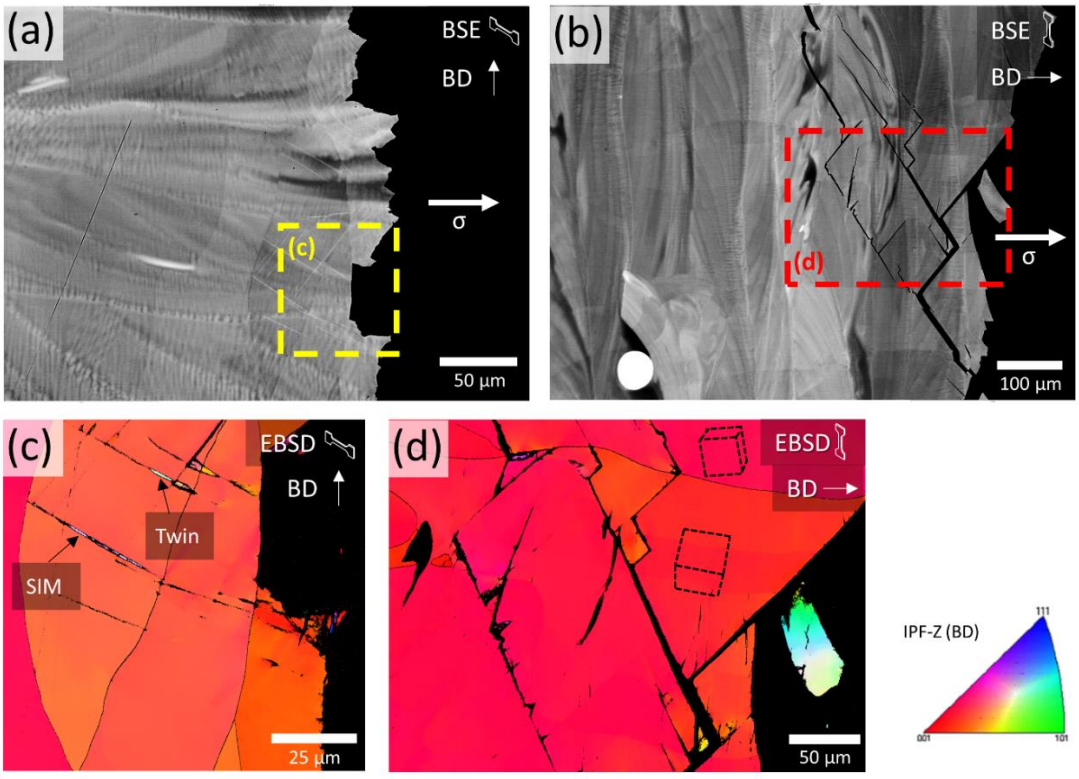

Figure 10. Micrographs on the side surface of tensile-tested (a) horizontal and (b) vertical specimens, and (c) and (d) respective EBSD maps taken from the regions highlighted by the boxes in (a) and (b). Crystallographic orientations of each grain are displayed.

3.4. Fatigue crack growth

Results of the FCG tests on L, ⊥ and ∥ Ti41Nb specimens are displayed in Figure 11 as *da/dN* vs. Δ*K* plots. Values of *m* and ΔK_o extracted from them are summarized in Table 3. The FCG responses in ⊥ and ∥ orientations are similar, while those of L orientation are distinct. The *m* value in the latter is ~4.0, while it is ~2.8 and ~2.9 in the ⊥ and ∥ specimens, respectively, implying significant anisotropy. ΔK_o in L specimen is ~4.3 MPa√m, whereas it is ~3.7 and ~4.1 MPa√m in ⊥ and ∥ specimens, respectively. These differences manifest in a crossover in the FCG rates at ~6.5 MPa√m. For Δ*K* higher than this value, higher *m* in L specimen results in higher *da/dN*, in comparison to ⊥ and ∥ specimens.

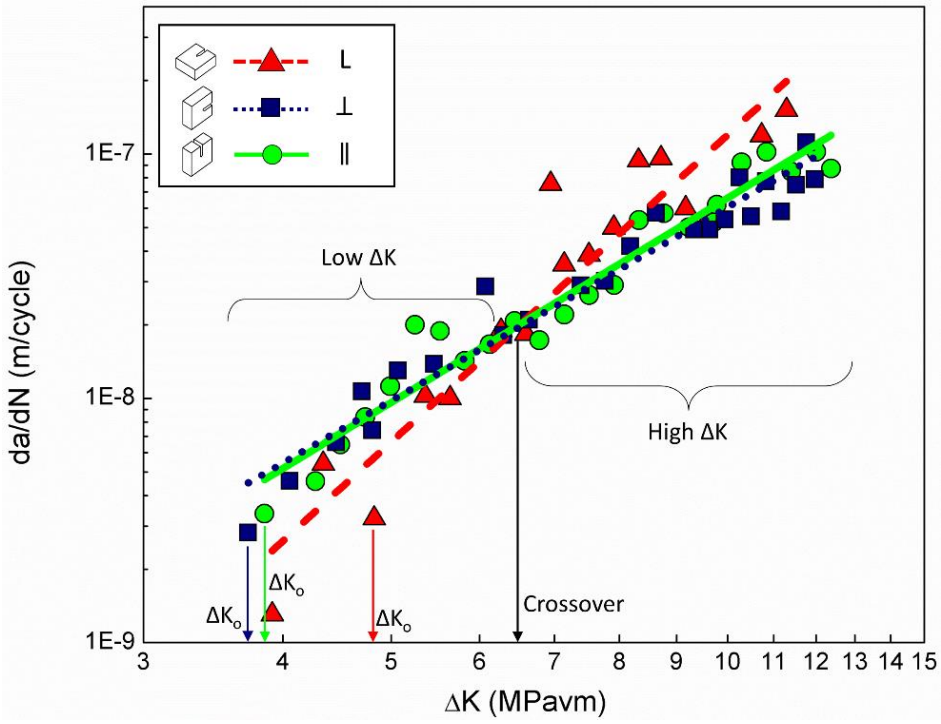

Figure 11. Representative Paris curve for L, ⊥ and ∥ CT specimen, where fatigue crack growth rate per cycle, da/dN, is plotted as a function of the applied stress intensity factor range, ΔK, in each sample. Upon reducing ΔK until the da/dN value is below 4x10^{-9} m/cycle, ΔK_o can be determined, as shown by the 3 arrows labelled with ΔK_o.

Table 3 Summary of the FCG properties and fracture toughness of in-situ alloyed Ti41Nb in 3 orientations, based on the experiments conducted on CT specimens. The data in parenthesis indicates the values obtained from individual experiment.

Orientation	**ΔK_0 (MPa√m)**	***m***	**$r_{max,planestrain}$ (µm)**	**K_{IC} (MPa√m)**
L	4.3 (3.8, 4.8)	4.0 (4.2, 3.9)	3.75 (2.90, 4.61)	37.5 (38.1, 36.8)
⊥	3.7 (3.7, 3.7)	2.8 (2.9, 2.6)	2.94 (2.93, 2.95)	22.6 (26.3, 19.0)
∥	4.1 (3.9, 4.4)	2.9 (2.8, 3.0)	3.37 (2.93, 3.82)	41.2 (41.8, 40.6)

Representative EBSD band contrast maps of L, ⊥ and ∥ specimens encompassing the fatigue pre-crack region are displayed in Figure 12. Corresponding to the cross-over value of ΔK, an indicative cutoff line was drawn on Figure 12 to separate the high and low ΔK region. In the high ΔK region, the crack path in the L specimen is relatively less tortuous, whereas ⊥ and ∥ specimens exhibit branching and tortuosity. In the low ΔK region, the fatigue crack in all the specimens transitioned into faceted/serrated crack growth mode, with L sample exhibiting the most serrated characteristic. The observed crack growth behavior of ⊥ and ∥ specimens agrees well with their corresponding Paris curves.

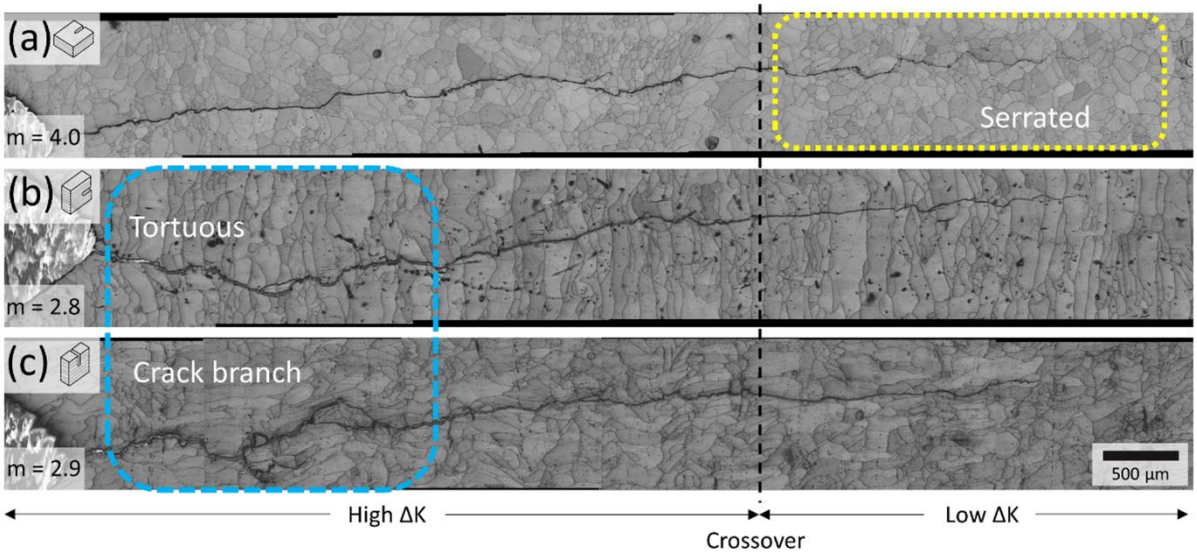

Figure 12. EBSD band contrast maps on the fatigue pre-cracked regions of (a) L (b) ⊥ and (c) ∥ CT specimen.

The FCG characteristic of L, ⊥ and ∥ specimens in the high Δ*K* region was observed using BSE in SEM (see Figure 13), to reveal the interaction of the crack with micro- and meso-structure of the material. Banded mesostructure could not be observed on the surface of L specimen, as the surface plane is perpendicular to BD. Minute amount of slip traces were formed in the vicinity of crack (indicated by white arrow in Figure 13a). As seen in Figure 13b and c, the crack propagation in the ⊥ and ∥ orientations in the high Δ*K* region is accompanied by markedly more slip traces than that in the L specimen. Higher magnification images from the regions of Figure 13b and c using secondary electron (SE) signal are displayed in Figure 13d and e, respectively, to aid the differentiation of slip traces and secondary cracks. The latter features can be identified, with the aid of "edge" effect commonly associated with SE imaging, for having two edges while the slip steps have only a single edge. The slip traces in these specimens are predominantly associated with NPR, indicating slip is relatively easier in these regions. It is not possible to pinpoint an accurate composition for the region due to the limited resolution of EDS and inhomogeneity. Nevertheless, a good estimation of Nb content in the NPR is ~33.1%.

The crack propagation in the specimens were preceded by one or multiple slip lines, which may form in single or multiple directions. In the case of the L specimen, short planar slip traces typically form ahead of the crack tip at 45^{o} relative to the mode I propagation direction. The crack propagates either in a sawtooth-like fashion (indicated by the red box in Figure 13a) or smooth planar crack. In contrast, crack propagation in the ⊥ and ∥ specimens was accompanied by predominant planar slip traces in multiple directions in NPR. The crack tends to grow along one of those slip traces until it gets arrested, followed by crack propagation in slip traces of alternative directions. This led to substantial crack branching and deflection, as seen in Figure 13b and c. On the occasion where the crack front meets a Nb particle, the delamination of the particle led to a large deviation from mode I crack growth direction, as seen in Figure 13c. Such a deviation results in the reduction of the driving force experienced by the crack tip for mode I crack growth, hence favoring branching of it. In all cases, there was negligible interaction between the crack and the melt pool boundaries.

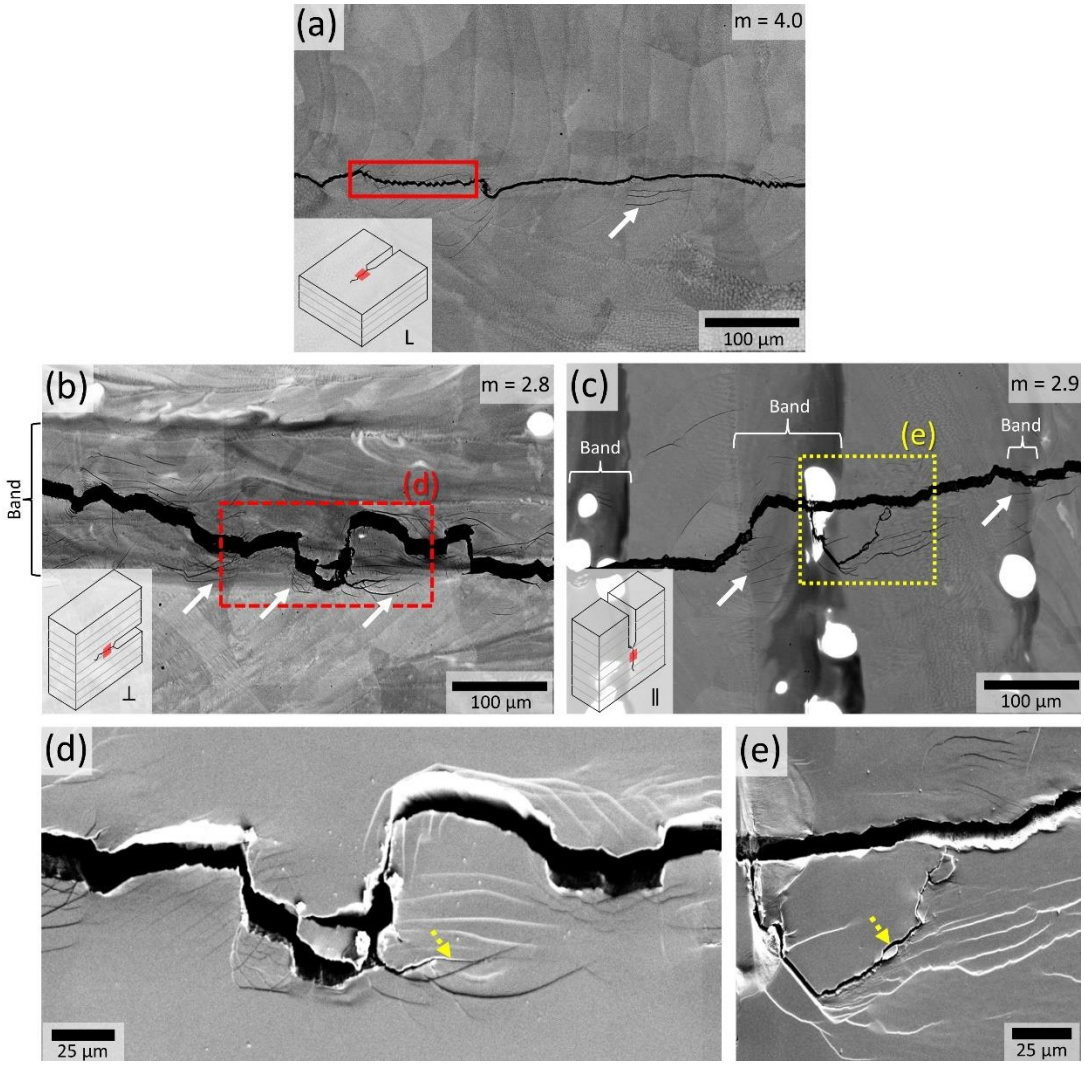

Figure 13. BSE micrographs of the high ΔK fatigue precracked region of (a) L (b) ⊥ and (c) ∥ CT specimens. Figures (d) and (e) are the magnified SE images of (b) and (c) respectively, which aid in the differentiation of secondary cracks and slip traces. White arrows in (a), (b) and (c) point the slip traces. Yellow discontinuous arrows in (d) and (e) point the secondary cracks. The red box in (a) indicates the sawtooth-like crack. Red shading on CT specimen illustration located at the bottom left corner of (a), (b) and (c) shows the location from which the micrographs are taken.

Optical micrographs of the fatigue fractured surfaces, including the low Δ*K* region, are shown in Figure 14. The L specimen is comprised of a highly serrated fracture surface, Figure 14a. The tortuous fracture surface is made up of cleavage planes that appear jagged in the direction perpendicular to the crack growth. On the other hand, the fracture surface for ⊥ specimen (Figure 14b) consists of cleavage planes with random and equiaxed character. Similarly, the

fracture surface of ∥ specimen exhibits random cleavage planes that are slightly elongated towards the direction of crack propagation (Figure 14c). In general, fracture surface features in all the specimens strongly resemble that of the grain morphology. The fracture surface characteristic of the L specimen is found to be consistent with the tortuous FCG characteristic in the low ΔK region, as observed from the side surface (Figure 12).

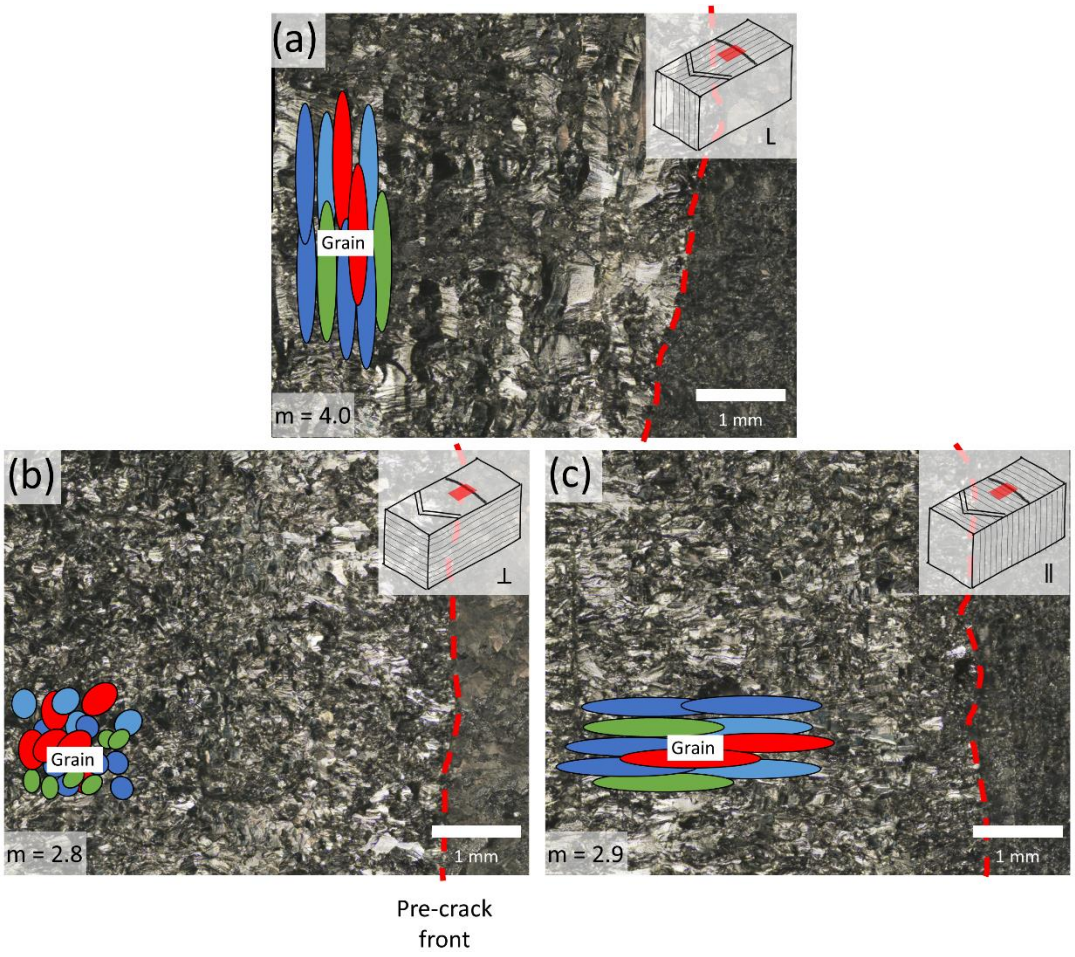

Figure 14. Optical micrographs of the fatigue fractured surfaces of (a) L (b) ⊥ and (c) ∥ specimens. The shaded region on the illustration of CT specimen located at the top right corner of each image shows the location where the fractograph is taken from. The representative illustration of grains in each image is for the purpose of visualizing the fracture surface formation with respect to grain character.

3.5. Fracture Toughness

Measured values of the mode I fracture toughness, $K_{IC,}$ are given in Table 3. Representative fracture surface corresponding to each specimen from the overloaded fracture region are illustrated in Figure 15. Amongst the three orientations investigated, the ⊥ specimens have the

lowest K_{IC} of 22.6 MPa√m. This is in agreement with their nearly-elastic stress-strain response with minimal plasticity. It is also similar to that reported (~22 MPa√m) for the Ti-15Mo (wt %) β-Ti alloy containing the ω_{iso} phase [44]. The poor fracture toughness is accompanied by a flat fracture surface in the fast fracture region (Figure 15b). The L and ∥ specimens, exhibit much higher K_{IC} (~37.5 and ~41.2 MPa√m, respectively) despite the poor tensile ductility observed in them during the tensile testing. The relatively higher toughness can be related to the tortuous fracture surfaces especially in the regions immediately ahead of the fatigue pre-crack fronts (see Figure 15a and c). The crack deflections are largely associated with the layers of NPR (depicted by yellow arrows), indicating a role of layered mesostructures in the toughening of the *in-situ* alloyed Ti41Nb. The as-built Ti41Nb parts demonstrated large anisotropy in their fracture response despite the similarity in tensile stress-strain response along different orientations.

To address the any concerns about the statistical significance of the small difference between mean K_{IC} values of ∥ and L specimens (3.75 MPa√m), one-tailed two-sample t-test was conducted on the data obtained in the two orientations. It was found that the ∥ orientation (μ = 41.2, σ = 0.849) as compared to the L orientation (μ = 37.5, σ = 0.919) demonstrated significantly better K_{IC}, $t(2)$ = 2.92, *p-value* = .025696. (*p-value* is the probability that the results from the sample data occurred by chance). The details of the calculations can be found in the Supplementary Information.

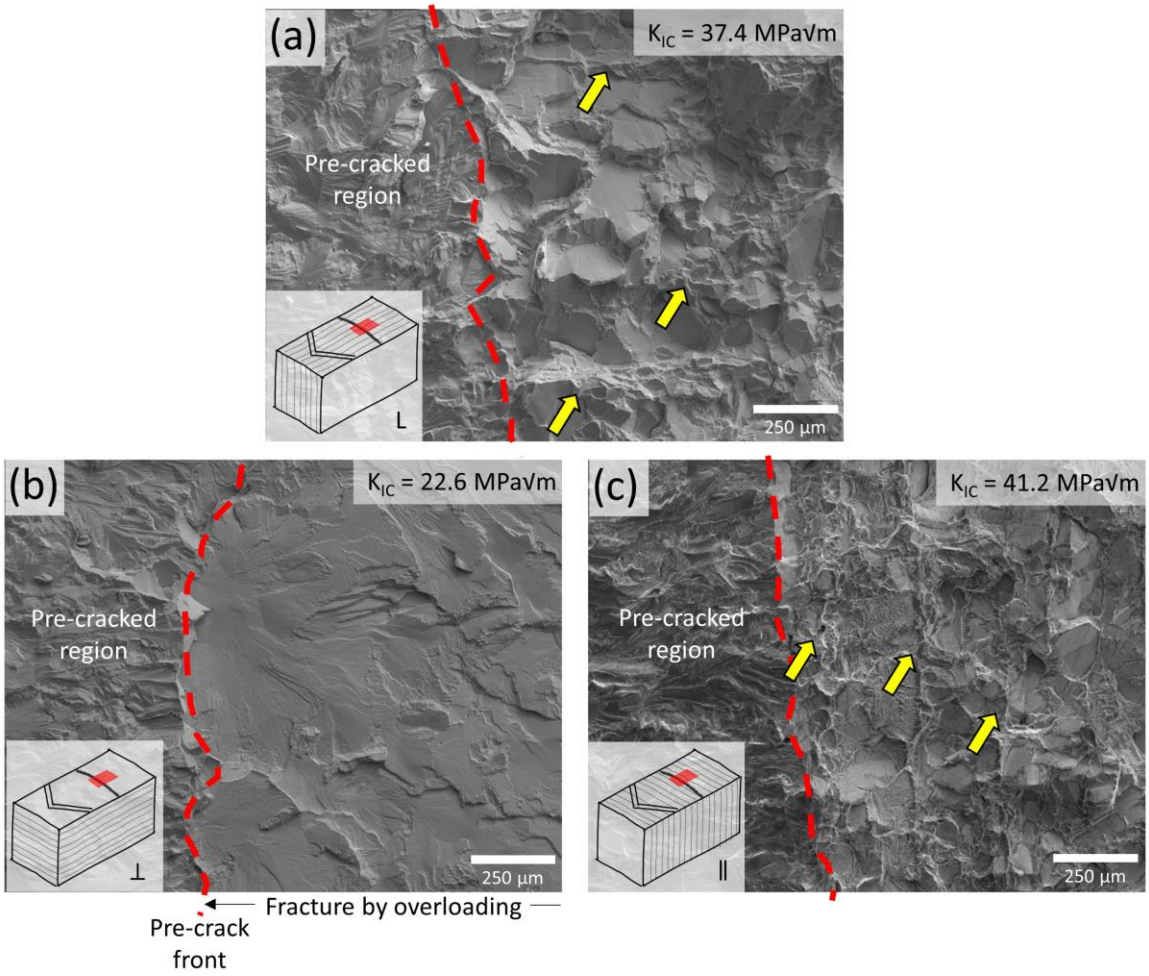

Figure 15. Fractographs of the fast fracture regions of (a) L, (b) ⊥, and (c) ∥ specimens. The shaded region on the illustration of CT specimen located at the bottom left corner of each image shows the location where the fractographs were taken from.

4. Discussion

4.1. Composite effect of in-situ alloying

The inherently fast cooling rate associated with the LB-PBF process leads to a short residence time of materials in the melt and the consequent incomplete melting and diffusion of Nb. As the melt pool forms, the relatively heavier Nb particles tend to settle at the bottom of the melt pool. Subsequent freezing of Nb particles near the melt pool boundary results in the formation of partially molten Nb particles. Without sufficient supply and diffusion of Nb, NPRs form around the Nb particles. Subsequent laser hatch remelts a portion of the melt pool side boundary, leaving the bottom of the melt pool as NPR. The upper region of a melt pool has relatively more time available for Nb diffusion and homogenization, thereby forming the matrix region

with close-to-nominal composition. As a result of this, mesostructured built-parts with alternative layers of Nb-poor and nominal matrix regions are formed, as depicted by the lines in the schematic of the CT specimens (Figure 2a). In reality, the layered structure is not perfect as NPR can spread across a layer, but might not occupy the entire layer.

As discussed already, the formation of ω_{iso} phase suppresses dislocation mediated plasticity in the matrix region. In contrast, it appears that the NPR is able to accommodate more plasticity through dislocation slip, as seen from Figure 13b and c. Thus, the layered structure can be viewed—in an approximate fashion—as a composite with alternative soft and hard regions. Consequently, it exerts a large influence on the mechanical behavior, especially the FCG and fracture responses, as discussed below.

4.1.1. Fatigue crack growth mechanisms

The FCG characteristics of *in-situ* alloyed Ti41Nb are strongly affected by the layered mesostructure, with NPR causing a strong specimen orientation-dependent crack growth behavior. Schematic illustrations of the different crack growth mechanisms in the high ΔK regime, i.e., steady state crack growth region, for different orientations are provided in Figure 16.

Assuming elastic-perfectly plastic behavior, which is reasonable considering the negligible work hardening behavior of Ti41Nb, the maximum plastic zone size, r_{max}, of Ti41Nb at any ΔK under plane strain conditions and within the continuum mechanics framework is given as $r_{max,planestrain} = \frac{1}{3\pi}\left(\frac{\Delta K}{(1-R)YS}\right)^2$ [45]. While the plane strain condition holds for the majority of samples' thickness, the samples' surfaces were under plane stress condition. Hence, surface observation should correspond to plane stress r_{max}, given as $r_{max,planestress} = \frac{1}{\pi}\left(\frac{\Delta K}{(1-R)YS}\right)^2$ [45]. For ΔK = 11 MPa√m, which corresponds to high ΔK region, $r_{max,planestrain}$ for L, ⊥ and ∥ specimens are ~23.9, ~25.7 µm and ~23.9 µm, respectively. Meanwhile, the $r_{max,planestress}$ are ~71.8, ~77.2, and ~71.8 µm, respectively (simply multiplying $r_{max,planestrain}$ by a factor of three). All these are much smaller than the average grain width of 148.9 µm. For the L specimen, the large grain size in comparison to $r_{max,planestress}$ led to slip traces only near the crack tip upon cyclic loading. These slip traces typically formed in two orthogonal directions along {112} planes and were approximately 45° to the Mode I FCG direction. The angle of slip traces corresponds to the maximum shear stress direction ahead of the crack tip under mode I loading

condition. The crack propagates in a sawtooth-like fashion as seen in Figure 13a, which can be explained by the single crystal crack growth model [46], owing to the relatively large grain size in the material. In that model, the work hardening of one slip plane leads to alternating shear on another. Due to the kinematic irreversibility of cyclic slip, net planar crack growth occurs along the intersecting line of two slip planes. It should also be noted that the observed slip traces were generally within ~25 μm around the crack, despite having $r_{max,planestress}$ of 71.8 μm. The relatively limited formation of slip traces indicates that r_{max} values in matrix region may be overestimates. The calculation of r_{max} values are based on the tensile data that encompasses the contribution from both matrix and NPR. Since the yield strength of the matrix region alone could not be obtained, accurate estimate of r_{max} values within it could not be made.

As for the ⊥ specimen, $r_{max,planestress}$ of 77.2 μm corresponds well with the observed zone of the slip trace formation. Dominant slip traces which span a few grains away from the crack front when the crack is in NPR were also observed. These slip traces can be wavy and are not necessarily orientated at 45^{o} to the mode I direction, owing to the change in maximum shear stress direction when the slip line is away and at an angle from the mode I crack growth direction. Similar to the L sample, fatigue cracks propagate along the slip traces in the ⊥ specimen. The slip traces were generally along one direction within a grain and changed direction across grain boundaries, leading to crack propagation with severe deflections. In addition, the Nb distribution in NPR is inhomogeneous, and the crack propagation can occasionally get blocked by the localized Nb-rich region. Thus, NPR can be viewed as a maze for the crack, inducing crack tortuosity that deviates the crack from mode I propagation direction which effectively reduces its growth rate. It was also noted that crack tends to move towards NPR, possibly because it is easy to form slip traces in this region, which effectively provides easier path for crack growth, though once crack growth initiates in this region these slip traces results in tortuosity, as previously discussed.

In the ∥ specimen, the spatial arrangement of layered composite mesostructure (as indicated in Figure 16) gave it a different FCG characteristic at high ΔK. The propagating crack encounters NPR “barriers” periodically. Since they have higher propensity of deforming plastically than the matrix region, crack deflection similar to that observed in the ⊥ specimen was observed. As the unmelted Nb particles are also present in NPR, the crack front also encountered Nb particles as it propagates. As the crack passes, the Nb particles delaminate from the matrix and

leading to deviation of the crack from the mode-I direction. This leads to a reduction in the crack tip driving force, crack arrest and branching, as illustrated schematically in Figure 16. Crack branching results in a reduced FCG rate. Such crack branching can also be seen in ⊥ sample but with less frequency, since the chance of encountering a Nb particle is lesser in this orientation.

One may argue that the L specimen has layers of NPR parallel to the crack growth direction, thus, it should have induced tortuous FCG and crack branching. However, unlike other specimens, NPR does not span the entire crack front in the L specimen. Hence, the effectiveness of NPR to promote crack tortuosity and branching in L is relatively insignificant.

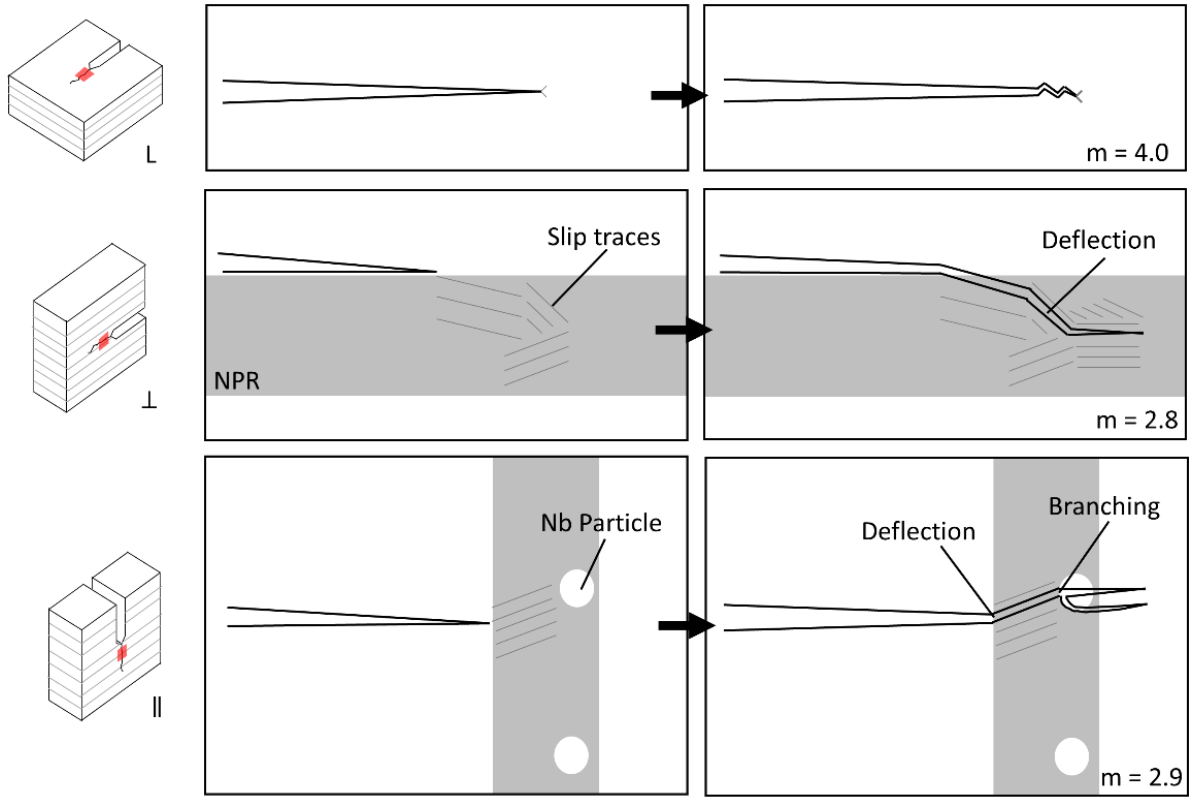

Figure 16. Schematic illustrations of the FCG mechanisms in the high ΔK region of L, ⊥ and ∥ CT specimens.

As the ΔK approaches ΔK_o, $r_{max,planestrain}$ approaches 2.9 – 3.7 µm for all specimens, hence the interaction of the crack with the mesostructure was limited. On the other hand, the microstructure plays a bigger role since the crack growth behavior shows dependence on the crystallographic/morphologic nature of the grains (see Figure 14). The morphology of the

grains dominated the FCG behavior at low ΔK, leading to anisotropic FCG response in the near threshold region. For the L specimen, the grains have their long axis arranged along the crack front. This minimized the crystallographic variation associated with crack growth in the L specimen, in contrast to the ⊥ and ∥ specimen, as depicted in Figure 14. Hence, the near-threshold crack in the L specimen experienced unfavorable condition for crack growth to form highly tortuous fracture surface, which significantly reduced the FCG rate through roughness-induced closure [45].

In summary, a transition from the crack interaction with mesostructure to microstructure was observed as ΔK was reduced, resulting in a variation in the FCG character. At high ΔK, NPR in ⊥ and ∥ specimens led to crack tortuosity and branching, which reduces the driving force for FCG. Near the threshold, the grain morphology promoted highly tortuous crack growth in the L specimen, causing roughness-induced closure that resulted in relatively higher ΔK_o. The change in the crack growth mechanism led to a crossover in the Paris curves, where L specimen exhibited a significantly higher m than that of ⊥ and ∥ specimen. This insight can be utilized for defect-tolerant-design of parts manufactured via the *in-situ* alloying route where the mesostructure could be engineered to induce resistance towards crack propagation.

4.1.2. Toughening mechanisms

Moving on to the quasi-static fracture response, the plane strain condition necessary for determining K_{IC} was satisfied in all the three different orientations, due to high YS and relatively low toughness of the as-built parts. The lack of K_{IC} data in literature for the β-Ti alloys makes it difficult to provide a direct comparison with CM/AM counterparts. It is noteworthy that K_{IC} in L and ∥ orientations is nearly-double that in ⊥ orientation. This is due to the crack deflection induced by the layered composite mesostructure in the former two cases (Figure 15a and c). The propagating crack gets deflected from its nominal mode I growth direction at the interfaces of the soft/hard regions. Under the same far field $K_{I,}$ the effective driving force for a deflected crack is typically smaller than that of a straight crack of the same projected length [45]. As such, a larger far-field stress is required to fracture a specimen with deflected crack in comparison to a straight crack. Consequently, the layered mesostructure enhances the toughness in L and ∥ orientations, even though they show limited plasticity. This further highlights the importance to evaluate the fracture toughness of AM alloy instead of only relying on the uniaxial tension properties. Schematic illustrations of the fracture mechanisms

in different orientations are displayed in Figure 17a. A representative side surface of the fractured specimen showing the crack deflection caused by the soft and hard layers in the ∥ specimen is displayed in Figure 17b.

The fracture behavior of *in-situ* alloyed Ti41Nb observed in the present study illustrates that the multiscale micro- and mesostructures can be designed and incorporated into AM parts to realize extrinsic toughening ahead of a crack to achieve higher fracture resistance. In the case of LB-PBF, the unique ability to induce several different types of mesostructure can be leveraged to resist fracture. For instance, wavy melt pool boundary induced by multiple laser scans imparted high crack tortuosity and toughened the resultant material, as seen in the case of Al12Si, AlSi10Mg and Al-Mg-Sc-Zr alloys [17, 18, 47]. Similarly, when the crack propagation direction is perpendicular to the BD, prior β columnar grains in Ti6Al4V induce tortuosity and toughened the material [19]. For Fe19Ni5Ti (wt%) maraging steel fabricated via DED, incorporation of periodic pauses enables *in-situ* martensite formation, which is essential to trigger hard η-phase precipitation via subsequent intrinsic heat treatment [48]. When properly planned, Damascus-like banded mesostructure with alternating hard and soft layer can be obtained, which results in Charpy impact toughness improvement. Extrinsic toughening mechanisms seems to be an interesting consequence of laser AM which needs to be explored further in the future, because a high fracture toughness was obtained in all the above-mentioned cases without sacrificing the strength. Since LB-PBF is a near net shape processing technology, and hence does not require further forming procedure, fracture toughness can be a more important mechanical property of relevance in engineering design in comparison to ductility. It is possible to further enhance K_{IC} of the specimen by incorporating NPR in a controlled fashion and informed by fracture mechanics, i.e., based on the maximum plastic zone size, cyclic plastic zone size, etc. One way is to selectively scan and melt the powder bed with a checkerboard pattern of alternating high and low E_d regions. This, in turn, can create alternate regions of matrix and NPR across the same layer, which effectively toughens the resultant part in all directions, possibly resulting in isotropic properties. The inherently fast cooling cycle and flexibility of LB-PBF process enables the possibility of designing mesostructure in controlled fashion to obtain desired properties. While the AM processes offers tremendous opportunity to design and tailor materials, the feat remains challenging due to the need of considering all the factors.

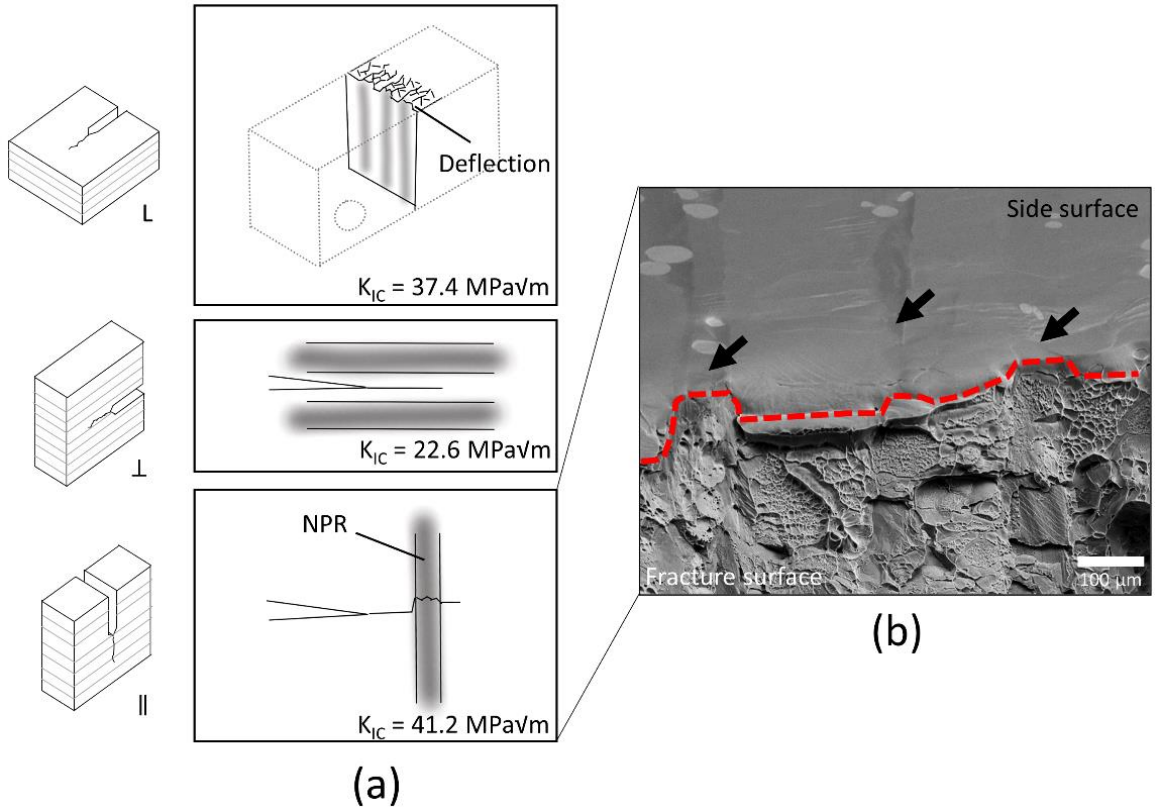

Figure 17 (a) Schematic diagrams showing the fast fracture behavior of L, ⊥ and ∥ CT specimens. (b) An SEM image illustrating the effect of NPR on crack deflection in ∥ orientation. Black arrows point toward bands of NPR. The dashed line traces the boundary of the fast fracture region.

4.2. Build size effects

We now turn our attention to the unusual existence of ω_{iso} phase in the *in-situ* alloyed Ti41Nb. In fact, the composition of 41 wt.% of Nb was selected on the basis of a past study where similar range of Nb addition led to a β-Ti alloy with the combination of lowest E ~57 GPa, moderate YS ~600 MPa and reasonable ε_f ~13% [40]. In another study on LB-PBF manufactured Ti42Nb (wt.%) using pre-alloyed powder, properties of E ~60.5 GPa, YS ~674.1 MPa and ε_f ~11.6% were reported [12]. Therefore, the cause for the brittleness exhibited by the alloy of the present study, specifically the origins of ω_{iso} phase, mandated further investigation.

During the LB-PBF process, considerable heat accumulation can occur, which leads to a significant increase in the temperature of the part-in-progress; the increase would be commensurate with the number of build layers [49]. It was shown that for 316L steel, the part's temperature at the top surface can reach ~250 and 500 ^{o}C for a total 300 and 1000 layers built,

respectively. Since Ti41Nb's thermal conductivity is similar to that of 316L, an analogous temperature increase during its LB-PBF can be anticipated. In this study, at least 600 build layers were required to build the CT specimens. This could easily bring the surface temperature of the specimens to above 250 ^{o}C. (The LB-PBF machine used for printing the coupons examined in this study was not equipped with *in-situ* temperature monitoring device, for us to confirm this.) Moreover, the high E_d required for homogenization of *in-situ* alloyed component in this study (410 J/mm^3) could exacerbate the heat accumulation, as opposed to that required for pre-alloyed Ti42Nb (40 J/mm^3) [12] or 316L stainless steel (48.5 J/mm^3) [49]. Since, precipitation of ω_{iso} was reported at temperatures as low as ~250 ^{o}C [29], it is not surprising to find it in the Ti41Nb alloy due to the effect of heat accumulation. Thus, the lack of ductility in the built parts could simply be due to their size.

To ascertain the above, parts with relatively small build size of 12 mm (width) x 30 mm (length) x 7 mm (height) were built with the H20 parameter. Additionally, one of the large part was solution heat treated (at 750 °C, which is above the Ti41Nb β-transus temperature for an hour followed by water quenching) to examine if ductility of large builds can be restored by a post-fabrication heat treatment. Representative tensile stress-strain responses of the specimens tested in the horizontal orientation are displayed in Figure 18, and properties extracted from them are summarized in Table 4.

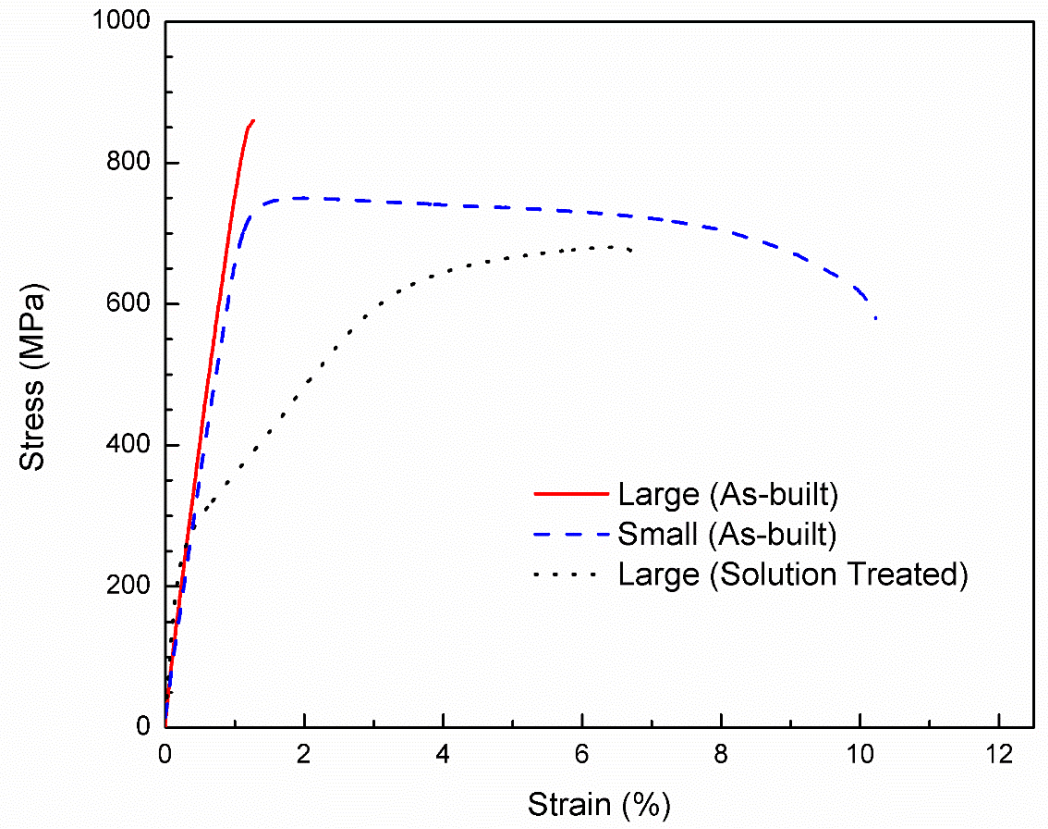

Figure 18 Representative tensile stress-strain responses of the large, small, and solution treated large samples; all tested in the horizontal orientation.

Table 4 Tensile properties of horizontal tensile coupon extracted from large, small and solution treated large sample. When applicable, the values are quoted with confidence interval of 99.7%. The data in parenthesis indicates the values obtained from individual experiment.

Sample	**YS (MPa)**	**UTS (MPa)**	***E* (GPa)**	**e_f (%)**
Large	785 ± 31.6	787 ± 32.0	74.1 ± 8.5	1.7 ± 0.5
Small	751 ± 3.5	N/A	66.0 ± 15.7	13.3 ± 4.8
Solution Treated	321 ± 90.3	684 ± 5.1	113.9 (103.5, 124.3)	10.7 ± 6.2

A significantly improved e_f of ~13.3%, with a YS that is only ~5% lower than that of the Large sample, was noted for the as-built small Ti41Nb part. A marked reduction in *E* to ~66 GPa was also observed. These improvements confirm the detrimental build size effect associated with Ti41Nb alloy, or metastable β-Ti in general. While the solution treatment of the Large part enhanced e_f to ~10.7%, a substantial reduction in YS was noted. Its stress-strain response

indicates to the SIM formation, which could be the reason for the significant reduction in its YS. Large variations in the tensile properties were observed after solution heat treatment, which is possibly due to the compositional inhomogeneity in the *in-situ* alloyed part. Hence, heat treatment for *in-situ* alloyed Ti41Nb needs to be further optimized despite the improved ductility, which is however not within the scope of this study.

The above results show that a detailed understanding of the build size effect is critical in ensuring the safety and reliability of as-built metastable β-Ti products. On that basis, several process related improvements are essential. The following are some suggestions. Firstly, actively cooled substrate platform can be employed to reduce heat accumulation, especially in the process of building a large structure. Care should be taken in the spatial orientation of a part to reduce the extend of heat accumulation, e.g., a solid component built on top of a lattice structure could lead to severe heat accumulation due to the poor heat conduction through the lattice structure. Monitoring of the temperature *in-situ* can aid in the product certification or process intervention when required. Time delay between scans can be adjusted to enable heat dissipation based on the monitored temperature data. From a practical and efficiency standpoint, time delay before next layer laser scanning can be implemented by increasing the number of parts within a same build job. Finally, a standardized heat treatment procedure should be developed to ensure reliable properties in the resultant part regardless of the build size.

Before closing, a brief discussion above the effect of porosity on the measured mechanical performance. A large number of studies on a wide variety of AM alloys have shown that porosity in the as-built parts is inevitable and exerts a large influence on the mechanical performance. The detrimental effect of the pores is particularly exacerbated especially when the ductility of the alloy is relatively low, as in the present case. However, the results obtained in this study show that they are not significantly affected by the porosity. This could be due to the fact that the porosity is low and/or pore sizes are sufficiently small that the microstructural effects play a predominant role. The most critical aspect, which controls the component's service life, that is affected by porosity is unnotched fatigue. We are currently investigating that aspect.

5. Summary and conclusions

The *in-situ* alloying approach was utilized to fabricate Ti41Nb blocks, whose microstructural and mechanical properties were characterized. The small *h* fast V_L strategy was employed to obtain parts with optimum combination of the amount of unmelted Nb (~0.391%) and porosity level (<0.5%). Following are the key findings of this study:

1) The mesostructure of the fabricated blocks comprises columnar grains and a 'composite' structure with NPR and matrix layers. Extensive nanoscale ω_{iso} precipitation, a result of the heat accumulation during processing due to the large build sizes, was observed.
2) Tensile testing showed that the as-built parts have YS > 780 MPa, E < 76.3 GPa, and ε_f < 1.65%. The low ductility was attributed to the existence of nano-sized ω_{iso} phase. The anisotropy in these properties was found to be insignificant.
3) The FCG rate at high ΔK was strongly influenced by the layers of NPR and hence depend on the orientation. In the ⊥ and ∥ orientations, a large extent of NPR ahead of the crack front led to crack deflection and lower FCG rates. The near-threshold FCG rate was strongly influenced by the local slip systems ahead of the crack. Highly serrated crack path that retards the crack was observed in the L orientation, as compared to those in the ⊥ and ∥ orientations.
4) The printed specimens exhibited significant anisotropy in terms of K_{IC}, with 22.6 MPa√m in ⊥ orientation being minimum and ~41.2 MPa√m in ∥ orientation being the maximum. Higher toughness in the L and ∥ orientations is aided by the interface between NPR and matrix region that promotes crack deflection.
5) Results of the small-sized parts and solutionized large parts demonstrated that the embrittlement of the large LB-PBF Ti41Nb is due to build size effect that was caused by heat accumulation that led to precipitation of the ω_{iso} phase.

Acknowledgement

This research is supported by the Agency for Science, Technology and Research (A*STAR) of Singapore via the Structural Metal Alloys Programme (No. A18B1b0061) and the National Research Foundation, Prime Minister's Office, Singapore under its Medium-Sized Centre funding scheme. S. Huang would like to acknowledge Nanyang President's Graduate Scholarship from Nanyang Technological University for funding the Ph.D. studies. Special

thanks are extended to Dr. Shihao Li for his help on TEM analysis and Mr. Siyuan Li for the invaluable scientific discussions.

References

[1] M. Niinomi, Y. Liu, M. Nakai, H. Liu, H. Li, Biomedical titanium alloys with Young's moduli close to that of cortical bone, Regen Biomater 3(3) (2016) 173-185.

[2] S.L. Sing, J. An, W.Y. Yeong, F.E. Wiria, Laser and electron-beam powder-bed additive manufacturing of metallic implants: A review on processes, materials and designs, Journal of Orthopaedic Research 34(3) (2016) 369-385.

[3] L. Yan, Y. Yuan, L. Ouyang, H. Li, A. Mirzasadeghi, L. Li, Improved mechanical properties of the new Ti-15Ta-xZr alloys fabricated by selective laser melting for biomedical application, Journal of Alloys and Compounds 688 (2016) 156-162.

[4] E.G. Brodie, A.E. Medvedev, J.E. Frith, M.S. Dargusch, H.L. Fraser, A. Molotnikov, Remelt processing and microstructure of selective laser melted Ti25Ta, Journal of Alloys and Compounds 820 (2020) 153082.

[5] S.L. Sing, W.Y. Yeong, F.E. Wiria, Selective laser melting of titanium alloy with 50 wt% tantalum: Microstructure and mechanical properties, Journal of Alloys and Compounds 660 (2016) 461-470.

[6] D. Zhao, C. Han, J. Li, J. Liu, Q. Wei, In situ fabrication of a titanium-niobium alloy with tailored microstructures, enhanced mechanical properties and biocompatibility by using selective laser melting, Materials Science and Engineering: C (2020) 110784.

[7] M. Fischer, D. Joguet, G. Robin, L. Peltier, P. Laheurte, In situ elaboration of a binary Ti–26Nb alloy by selective laser melting of elemental titanium and niobium mixed powders, Materials Science and Engineering: C 62 (2016) 852-859.

[8] D. Zhao, C. Han, Y. Li, J. Li, K. Zhou, Q. Wei, J. Liu, Y. Shi, Improvement on mechanical properties and corrosion resistance of titanium-tantalum alloys in-situ fabricated via selective laser melting, Journal of Alloys and Compounds 804 (2019) 288-298.

[9] H. Liang, D. Zhao, X. Feng, L. Ma, X. Deng, C. Han, Q. Wei, C. Yang, 3D-printed porous titanium scaffold incorporating niobium for high bone regeneration capacity, Materials & Design (2020) 108890.

[10] R. Duan, S. Li, B. Cai, Z. Tao, W. Zhu, F. Ren, M.M. Attallah, In situ alloying based laser powder bed fusion processing of β Ti–Mo alloy to fabricate functionally graded composites, Composites Part B: Engineering (2021) 109059.

[11] M. Simonelli, N.T. Aboulkhair, P. Cohen, J.W. Murray, A.T. Clare, C. Tuck, R.J.M. Hague, A comparison of Ti-6Al-4V in-situ alloying in Selective Laser Melting using simply-mixed and satellited powder blend feedstocks, Materials Characterization (2018).
[12] C. Schulze, M. Weinmann, C. Schweigel, O. Keßler, R. Bader, Mechanical Properties of a Newly Additive Manufactured Implant Material Based on Ti-42Nb, Materials 11(1) (2018) 124.
[13] J.C. Wang, Y.J. Liu, P. Qin, S.X. Liang, T.B. Sercombe, L.C. Zhang, Selective laser melting of Ti–35Nb composite from elemental powder mixture: Microstructure, mechanical behavior and corrosion behavior, Materials Science and Engineering: A 760 (2019) 214-224.
[14] Z. Sun, X. Tan, S.B. Tor, W.Y. Yeong, Selective laser melting of stainless steel 316L with low porosity and high build rates, Materials & Design 104 (2016) 197-204.
[15] T.H. Becker, P. Kumar, U. Ramamurty, Fracture and fatigue in additively manufactured metals, Acta Materialia 219 (2021) 117240.
[16] E.G. Brodie, J. Richter, T. Wegener, T. Niendorf, A. Molotnikov, Low-cycle fatigue performance of remelted laser powder bed fusion (L-PBF) biomedical Ti25Ta, Materials Science and Engineering: A 798 (2020) 140228.
[17] J. Suryawanshi, K.G. Prashanth, S. Scudino, J. Eckert, O. Prakash, U. Ramamurty, Simultaneous enhancements of strength and toughness in an Al-12Si alloy synthesized using selective laser melting, Acta Materialia 115 (2016) 285-294.
[18] M.J. Paul, Q. Liu, J.P. Best, X. Li, J.J. Kruzic, U. Ramamurty, B. Gludovatz, Fracture resistance of AlSi10Mg fabricated by laser powder bed fusion, Acta Materialia 211 (2021) 116869.
[19] P. Kumar, U. Ramamurty, Microstructural optimization through heat treatment for enhancing the fracture toughness and fatigue crack growth resistance of selective laser melted Ti6Al4V alloy, Acta Materialia 169 (2019) 45-59.
[20] ASTM B348 / B348M - 19, Standard Specification for Titanium and Titanium Alloy Bars and Billets, ASTM International, West Conshohocken, Pennsylvania, 2019.
[21] A.M. Mancisidor, F. Garciandia, M.S. Sebastian, P. Álvarez, J. Díaz, I. Unanue, Reduction of the Residual Porosity in Parts Manufactured by Selective Laser Melting Using Skywriting and High Focus Offset Strategies, Physics Procedia 83 (2016) 864-873.

[22] S. Huang, R.L. Narayan, J.H.K. Tan, S.L. Sing, W.Y. Yeong, Resolving the porosity-unmelted inclusion dilemma during in-situ alloying of Ti34Nb via laser powder bed fusion, Acta Materialia 204 (2021) 116522.
[23] T. Mishurova, K. Artzt, J. Haubrich, G. Requena, G. Bruno, New aspects about the search for the most relevant parameters optimizing SLM materials, Additive Manufacturing 25 (2019) 325-334.
[24] ASTM E8 / E8M-21, Standard Test Methods for Tension Testing of Metallic Materials, ASTM International, West Conshohocken, Pennsylvania, 2021.
[25] ASTM E399-12, Standard Test Method for Linear-Elastic Plane-Strain Fracture Toughness K Ic of Metallic Materials, ASTM International, West Conshohocken, Pennsylvania, 2012.
[26] ASTM E647-15, Standard Test Method for Measurement of Fatigue Crack Growth Rates, ASTM International, West Conshohocken, Pennsylvania, 2015.
[27] S.L. Sing, S. Huang, G.D. Goh, G.L. Goh, C.F. Tey, J.H.K. Tan, W.Y. Yeong, Emerging metallic systems for additive manufacturing: In-situ alloying and multi-metal processing in laser powder bed fusion, Progress in Materials Science 119 (2021) 100795.
[28] W.E. King, H.D. Barth, V.M. Castillo, G.F. Gallegos, J.W. Gibbs, D.E. Hahn, C. Kamath, A.M. Rubenchik, Observation of keyhole-mode laser melting in laser powder-bed fusion additive manufacturing, Journal of Materials Processing Technology 214(12) (2014) 2915-2925.
[29] M. Bönisch, A. Panigrahi, M. Calin, T. Waitz, M. Zehetbauer, W. Skrotzki, J. Eckert, Thermal stability and latent heat of Nb–rich martensitic Ti-Nb alloys, Journal of Alloys and Compounds 697 (2017) 300-309.
[30] W. Chen, C. Chen, X. Zi, X. Cheng, X. Zhang, Y.C. Lin, K. Zhou, Controlling the microstructure and mechanical properties of a metastable β titanium alloy by selective laser melting, Materials Science and Engineering: A 726 (2018) 240-250.
[31] S. Huang, S.L. Sing, G. Delooze, R. Wilson, W.Y. Yeong, Laser powder bed fusion of titanium-tantalum alloys: Compositions and designs for biomedical applications, Journal of the Mechanical Behavior of Biomedical Materials (2020) 103775.
[32] M. Bönisch, M. Calin, T. Waitz, A. Panigrahi, M. Zehetbauer, A. Gebert, W. Skrotzki, J. Eckert, Thermal stability and phase transformations of martensitic Ti–Nb alloys, Science and technology of advanced materials 14(5) (2013) 055004.

[33] G.T. Aleixo, C. Afonso, A. Coelho, R. Caram, Effects of omega phase on elastic modulus of Ti-Nb alloys as a function of composition and cooling rate, Solid State Phenomena, Trans Tech Publ, 2008, pp. 393-398.
[34] A. Devaraj, S. Nag, R. Srinivasan, R.E.A. Williams, S. Banerjee, R. Banerjee, H.L. Fraser, Experimental evidence of concurrent compositional and structural instabilities leading to ω precipitation in titanium–molybdenum alloys, Acta Materialia 60(2) (2012) 596-609.
[35] L. Zhang, R. Narayan, B. Sun, T. Yan, U. Ramamurty, J. Eckert, H. Zhang, Cooperative shear in bulk metallic glass composites containing metastable β-Ti dendrites, Physical review letters 125(5) (2020) 055501.
[36] L. Zhang, R.L. Narayan, H.M. Fu, U. Ramamurty, W.R. Li, Y.D. Li, H.F. Zhang, Tuning the microstructure and metastability of β-Ti for simultaneous enhancement of strength and ductility of Ti-based bulk metallic glass composites, Acta Materialia 168 (2019) 24-36.
[37] J.Y. Zhang, G.F. Chen, Y.Y. Fu, Y. Fan, Z. Chen, J. Xu, H. Chang, Z.H. Zhang, J. Zhou, Z. Sun, B.L. Shen, F. Sun, Strengthening strain-transformable β Ti-alloy via multi-phase nanostructuration, Journal of Alloys and Compounds 799 (2019) 389-397.
[38] R. Hermann, H. Hermann, M. Calin, B. Büchner, J. Eckert, Elastic constants of single crystalline β-Ti70Nb30, Scripta Materialia 66(3-4) (2012) 198-201.
[39] Q. Wang, C. Han, T. Choma, Q. Wei, C. Yan, B. Song, Y. Shi, Effect of Nb content on microstructure, property and in vitro apatite-forming capability of Ti-Nb alloys fabricated via selective laser melting, Materials & Design 126 (2017) 268-277.
[40] Y.-H. Hon, J.-Y. Wang, Y.-N. Pan, Composition/Phase Structure and Properties of Titanium-Niobium Alloys, MATERIALS TRANSACTIONS 44(11) (2003) 2384-2390.
[41] M.J. Lai, T. Li, D. Raabe, ω phase acts as a switch between dislocation channeling and joint twinning- and transformation-induced plasticity in a metastable β titanium alloy, Acta Materialia 151 (2018) 67-77.
[42] W. Chen, S. Cao, W. Kou, J. Zhang, Y. Wang, Y. Zha, Y. Pan, Q. Hu, Q. Sun, J. Sun, Origin of the ductile-to-brittle transition of metastable β-titanium alloys: Self-hardening of ω-precipitates, Acta Materialia 170 (2019) 187-204.
[43] J. Nejezchlebová, M. Janovská, H. Seiner, P. Sedlák, M. Landa, J. Šmilauerová, J. Stráský, P. Harcuba, M. Janeček, The effect of athermal and isothermal ω phase particles on elasticity of β-Ti single crystals, Acta Materialia 110 (2016) 185-191.

[44] A. Bowen, Effect of heat treatment on fracture toughness of a Ti-15Mo alloy, Metals Technology 5(1) (1978) 17-23.
[45] S. Suresh, Fatigue of materials, Cambridge university press1998.
[46] P. Neumann, Coarse slip model of fatigue, Acta metallurgica 17(9) (1969) 1219-1225.
[47] Z. Wang, X. Lin, N. Kang, Y. Wang, X. Yu, H. Tan, H. Yang, W. Huang, Making selective-laser-melted high-strength Al–Mg–Sc–Zr alloy tough via ultrafine and heterogeneous microstructure, Scripta Materialia 203 (2021) 114052.
[48] P. Kürnsteiner, M.B. Wilms, A. Weisheit, B. Gault, E.A. Jägle, D. Raabe, High-strength Damascus steel by additive manufacturing, Nature 582(7813) (2020) 515-519.
[49] R.J. Williams, A. Piglione, T. Rønneberg, C. Jones, M.-S. Pham, C.M. Davies, P.A. Hooper, In situ thermography for laser powder bed fusion: Effects of layer temperature on porosity, microstructure and mechanical properties, Additive Manufacturing 30 (2019) 100880.